

ETH Zürich, Department of Physics

OPTICAL TRAPPING IN A BUILD-UP CAVITY

Master Thesis

Supervisor:

Matteo Marinelli

Student:

Christoph Fischer

Prof. Jonathan Home
Institute for Quantum Electronics
ETH Zurich

Zurich, 30. April 2015

Abstract

In the present thesis the development of an optical ion trap was continued [M. Marinelli, Master Thesis, ETH Zurich (2014)]. A narrow linewidth Nd:YAG laser was frequency doubled in a quasi phase-matched crystal and partially stabilized to a high finesse build-up cavity. It could be shown that the locking time was limited by mechanical vibrations of the optical table, making either passive damping or active beam-pointing stabilization necessary.

Furthermore, a novel ion trap design, incorporating both static electric and optical potentials, was developed and simulated using a Verlet-type integrator for solving the classical equation of motion.

Acknowledgement

First and foremost I would like to thank Prof. Jonathan Home for giving me the opportunity to work on this exciting project in his group. I would also like to thank Matteo Marinelli and Frieder Lindenfelser for supervising and supporting me during the daily work in the lab and helping me with apparently “unsolvable” problems; Ursin Solèr for his technical experience and help; Matteo Marinelli and Vlad Negnevitsky for proof-reading; and, of course, all the other members of the TIQI group, making my stay very enjoyable.

Last but not least I would like to thank Dr. Edgar Fischer for awakening my interest in optics and sharing his immense knowledge.

List of Abbreviations

| | |
|--------|--|
| BEM | Boundary element method |
| CPLD | Complex programmable logic device |
| dc | Pseudonym for static electric potential |
| EOM | Electro-optic modulator |
| eom | equation of motion |
| FDM | Finite difference method |
| FEM | Finite element method |
| FSR | Free spectral range |
| hf | High finesse (optical cavity) |
| MOPA | Master oscillator power amplifier |
| Nd:YAG | Neodymium-doped yttrium aluminium garnet ($\text{Nd:Y}_3\text{Al}_5\text{O}_{12}$) |
| PCB | Printed circuit board |
| PCF | Photonic crystal fibre |
| PDE | Partial differential equation |
| PDH | Pound-Drever-Hall (locking scheme) |
| PPLN | Periodically polled lithium niobate (LiNbO_3) |
| PPLT | Periodically polled lithium tantalate (LiTaO_3) |
| QPM | Quasi phase matching |
| rf | Radio frequency |
| RMS | Root mean squared |
| SHG | Second harmonic generation |
| QED | Quantum electrodynamics |

Contents

| | | |
|----------|--|-----------|
| 1 | Introduction | 1 |
| 2 | The Radio Frequency Ion Trap | 2 |
| 2.1 | Trapping of Charged Particles | 2 |
| 2.1.1 | Ions in a Static Electric Potential | 2 |
| 2.1.2 | Ions in a Radio-frequency Field | 2 |
| 2.2 | Radio-frequency Ion Trap Simulation | 4 |
| 2.2.1 | Finite Element Method | 5 |
| 2.2.2 | Boundary Element Method | 5 |
| 2.2.3 | Benchmarking of FEM and BEM | 5 |
| 3 | Electro-Optical Trap Simulation | 9 |
| 3.1 | The Optical Dipole Trap | 9 |
| 3.2 | Geometry of the Electro-Optical Trap | 10 |
| 3.3 | Electro-Optical Trap Simulation | 12 |
| 3.3.1 | Numerical Solving of Equations of Motion: The Verlet Algorithm . | 12 |
| 3.3.2 | The Equation of Motion | 14 |
| 3.3.3 | Magnesium in an Optical Lattice | 17 |
| 3.3.4 | Simulation Results | 18 |
| 4 | Optical Setup | 22 |
| 4.1 | Second Harmonic Generation | 22 |
| 4.1.1 | Theory of Second Harmonic Generation | 23 |
| 4.1.2 | Quasi Phase Matching in Periodically Poled Lithium Tantalate . . | 24 |
| 4.1.3 | Experimental Setup and Results | 26 |
| 4.2 | High Finesse Cavity | 31 |
| 4.2.1 | Cavity Frequency Stabilization (Pound-Drever-Hall Locking) . . . | 31 |
| 4.2.2 | Experimental Setup | 32 |
| 4.2.3 | Results | 32 |
| 5 | Summary and Outlook | 36 |
| A | Appendix | 40 |
| A.1 | List of Lenses | 40 |
| A.2 | Transmission of a Polarizing Beamsplitter | 40 |
| A.3 | Interlock System | 41 |

1 Introduction

Efficient simulation of quantum systems on classical computers is in general not possible due to the exponential growth of the equation order that has to be solved [1]. Having on the other hand a fully controllable quantum system \mathcal{A} , as proposed by R.P. Feynman in 1981 [2], it is possible to simulate a different system \mathcal{B} by tuning the interaction in system \mathcal{A} correctly and then measuring a suitable observable [3].

Ion strings kept in radio-frequency traps offer a naturally strong interaction due to their Coulomb repulsion and can also be very well controlled by the use of lasers [4]. Therefore, they provide an ideal system for simulating of a wide range of Hamiltonians containing either spin-spin interaction like the Ising Hamiltonian [5] or spin-oscillator couplings encountered for example in the Jaynes-Cummings model in cavity QED [4].

More recently experiments have been conducted in which single ions were trapped in optical fields produced by strongly focused lasers [6], [7], [8], a technique used so far only for trapping of neutral atoms [9]. Such traps offer new possibilities for simulating hybrid systems simultaneously containing both neutral atoms and ions. Furthermore, thanks to the much lower heating rate of the ion, the regime of ultracold chemistry could become accessible [8].

In this thesis a narrow linewidth laser system was set up, whose eventual purpose will be trapping of ions in the Gaussian mode of an optical cavity. This work is based on previous results by M. Marinelli, showing that such a laser is necessary in order to couple light stably into a build-up cavity used for trapping [10]. Furthermore numerical simulations were carried out, investigating a novel type of trap utilizing static electric as well as optical fields to spatially confine ions.

The first chapter of this thesis introduces the theory of radio-frequency trapping of charged particles and presents two different methods for numerical calculation of the potential generated by the trap electrodes. Implementations of these two methods were then compared using analytically solvable electrostatic problems as a benchmark.

In the second chapter the methods used for simulating the electro-optic hybrid trap as well as the results are presented. Furthermore dipole trapping of quantum systems in general as well as its applications and advantages in ion trapping are discussed.

The last part of this thesis describes the experimental setup. The theory of second harmonic generation in periodically polled crystals is discussed, which was then used for the generation of a green light source, following the description in [11]. Finally, this laser was coupled into the build-up cavity designed by M. Marinelli. These results are presented in the last section.

2 The Radio Frequency Ion Trap

This chapter begins with an introduction to radio-frequency trapping of charged particles. Thereby the alternating electric field is replaced by an effective potential acting on the particle. This approximation greatly simplifies the analysis of ion traps, yielding most experimentally important parameters such as position of the potential minimum, depth of the trap and secular frequencies of the ion.

The second part of the chapter covers the numerical analysis of arbitrary ion trap geometries. A method for calculating the effective potential is presented and its implementation in two different numerical solvers is discussed. These implementations are then compared using two problems which possess analytical solutions.

2.1 Trapping of Charged Particles

Thanks to their strong interaction with an electric field, charged particles such as ions can be confined to precisely defined points in space with ease. Placing the particles in vacuum facilitates storing them for nearly infinite time in the trap. Furthermore, good controllability is achieved by the use of lasers, enabling their study with high precision as well as their use in quantum information experiments [12].

However, as it will be shown in the following, trapping with solely *static* (dc) fields is not possible. This problem can be overcome by either using *radio-frequency* (rf) fields (called a Paul trap) or a combination of static electric and magnetic fields (Penning trap) [13].

In this section the case of a static quadrupole potential generated by a linear Paul trap is studied. These results are then extended to an oscillating drive field, yielding a static approximation of the dynamic rf confinement in an ion trap. In the end a brief outlook to a more precise approach which involves solving of the so-called Mathieu equations is given.

2.1.1 Ions in a Static Electric Potential

Maxwell's first equation in vacuum implies that

$$\nabla \mathbf{E}(\mathbf{x}) = -\nabla^2 \Phi(\mathbf{x}) = 0 \quad (2.1)$$

Therefore, for a quadrupole potential of the form

$$\Phi(\mathbf{x}) = \frac{U_1}{2}x^2 + \frac{U_2}{2}y^2 + \frac{U_3}{2}z^2 \quad (2.2)$$

for example produced by a Paul mass filter [14], the Laplace equation $\Delta\Phi = 0$ imposes

$$U_1 + U_2 + U_3 = 0 \quad (2.3)$$

Thus, at most two directions can be confined by a static electric potential while the third is anti-confined, manifested in a negative value of U_i .

2.1.2 Ions in a Radio-frequency Field

A fully confining potential can be achieved by the use of rf drive fields instead of static potentials. In the case of the Paul trap depicted in Figure 2.1 the time-dependent potential is of the form [14]

$$\Phi_{rf}(\mathbf{x}, t) = \frac{U_r}{R^2}(x^2 - y^2) \cos(\Omega_{rf}t) \quad (2.4)$$

when the rf field is applied to two opposing electrodes while keeping the other two grounded. The coefficient U_r is proportional to the radial potential strength and R is the distance to the electrodes.

At each instance in time the dc potential is of the previously discussed form, and therefore only confining in at most two spatial dimensions. However, due to the change of sign of the cosine term, the anti-confining axis alternates periodically between the $\hat{\mathbf{x}}$ and $\hat{\mathbf{y}}$ axis.

The *equation of motion* (eom) of a charged particle in the Paul trap is given by the Lorentz force $F(\mathbf{x}, t) = qE(\mathbf{x}, t) = -q\nabla\Phi_{rf}(\mathbf{x}, t)$. In the radial direction it reads

$$m \frac{d^2 x_i}{dt^2} = \pm \frac{2U_r}{R} x_i \cos(\Omega_{rf} t) \quad (2.5)$$

where i denotes the equation in $\hat{\mathbf{x}}$ and $\hat{\mathbf{y}}$ direction, respectively.

Since the position of the ion can be assumed to be constant over one oscillation cycle of the rf drive, the eom can be integrated once, yielding the radial velocity of the ion

$$v_i(t) = \frac{dx_i}{dt} \approx \pm \frac{qU_r}{m\Omega_{rf}R} x_i \sin(\Omega_{rf} t) \quad (2.6)$$

The rf potential is confining only along one axis at each instance in time and therefore a confining static potential in the axial direction is allowed.

The same approximation as above can also be used for calculating the axial velocity $v_z(t)$. Now, the average kinetic energy of an ion in the Paul trap

$$\langle E_{kin} \rangle = \frac{1}{2} m \langle (\mathbf{v}(t))^2 \rangle \approx \frac{1}{2} m (\omega_r^2 (x^2 + y^2) + \omega_a^2 z^2) \equiv \Phi_{eff}(\mathbf{x}) \quad (2.7)$$

can be calculated. Here, ω_r and ω_a are called the *secular frequencies* of the ion which describe the oscillation of the ion in the rf field, similar to the trajectory of a harmonic oscillator. This is called the *adiabatic approximation* and the effective potential described by the mean kinetic energy is called the *pseudo-potential* [30].

It is important to note that the pseudo-potential is proportional to

$$\Phi_{eff}(\mathbf{x}) \propto \frac{1}{\Omega_{rf}^2} |\nabla \Phi_{dc}(\mathbf{x})|^2 \quad (2.8)$$

where $\Phi_{dc}(\mathbf{x}) \equiv \Phi_{rf}(\mathbf{x}, t = 0)$ is the static potential generated by the trap electrodes at the beginning of each oscillation cycle.

By tuning the potentials correctly, it is possible to achieve a pseudo-potential which is confining in all three spatial dimensions, that is, both secular frequencies are real and much smaller than the frequency of the rf drive, validating the approximation in equation (2.6).

Mathieu's Equation The equation of motion can also be solved analytically. By applying a change of variables, it can be brought to the form of the well-studied *Mathieu equation* of the form [15]

$$\frac{d^2 x_i}{d\zeta^2} + \left(a_i + 2q_i \cos(2\zeta) \right) x_i = 0 \quad (2.9)$$

A complete treatment can be found for example in [15], which leads to an important result: On top of the slow secular motion of the ion with a frequency ω_i there is an

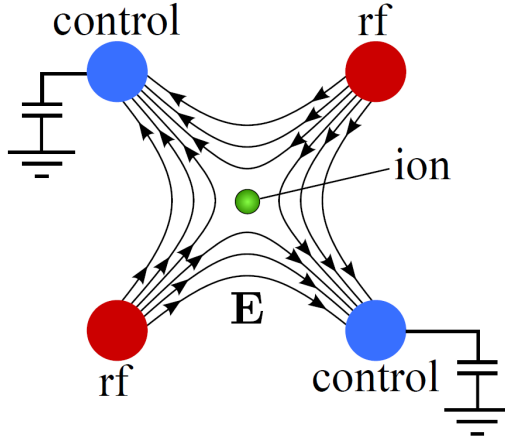


Figure 2.1: Geometry of the Paul trap. The two opposing rf electrodes are connected to an oscillating field while the remaining two electrodes are grounded. Image taken from [13].

additional modulation at the drive frequency Ω_{rf} and $2\Omega_{rf}$, i.e.

$$x_i(t) \approx A_i \left(\cos(\omega_i t + \phi_i) \left[1 + \frac{q_i}{2} \cos(\Omega_{rf} t + \frac{q_i^2}{32}) \cos(2\Omega_t) \right] + \beta_i \frac{q_i}{2} \sin(\omega_i t + \phi_i) \sin(\Omega_{rf} t) \right) \quad (2.10)$$

This is called the *micromotion* which leads to heating, i.e. an increase of kinetic energy of the ion. It is possible to minimize the micromotion [15], but it cannot completely compensated [16].

2.2 Radio-frequency Ion Trap Simulation

Solving Mathieu's equation for an arbitrary electrode geometry is complicated and the additional information that can be gained is very limited. To estimate the important trap parameters of a new trap geometry such as trap-depth and position of the potential minimum as well as of the required drive voltages and frequencies, it is sufficient to simulate the trap in the adiabatic approximation.

Since the time-averaged potential seen by the ion is solely determined by the dc potential of the trap electrodes (cf. equation (2.8)), it is sufficient to numerically find the static electric potential as well as the electric field generated by the trap electrodes.

Thanks to the linearity of electric potential and field, each electrode can be simulated individually with a test voltage of 1 V. In a second step, an arbitrary electrode configuration can be simulated by scaling each (pseudo-)potential accordingly. The total potential is then simply given by the sum of all individual potentials.

The static potential in free space generated by an electrode at a voltage U is determined by the solution of the Laplace equation

$$\Delta \Phi_{dc}(\mathbf{x}) = 0 \quad (2.11)$$

with Dirichlet boundary conditions $\Phi_{dc}^{(i)}(\mathbf{x}') = U$ for all points \mathbf{x}' lying on the surface of the electrode [19].

Many physical processes are described by *partial differential equations* (PDEs) like equation (2.11) and therefore a variety of computer programs exist for solving such problems. Most of these algorithms are either based on the *finite difference* (FDM), *finite element* (FEM) or *boundary element* (BEM) method [20].

In the following, the advantages and disadvantages of FEM, a very common all-purpose method, and BEM, a method particularly suited for solving electrostatic problems, are discussed.

2.2.1 Finite Element Method

Particularly in engineering the method of choice for simulating physical effects such as strain or temperature on components is FEM [13]. Thus, many highly optimized commercial products are available, providing many more simulation tools than are needed to solve the electrostatic problem imposed by the trap electrodes.

The FEM algorithm divides the whole space into a tetrahedral mesh – called finite elements. Then, the so-called *shape function* $W^{(i)}(\mathbf{x})$ is defined, which approximates the potential $\Phi_{dc}^{(i)}(\mathbf{x})$ piecewise on each tetrahedron i . By minimizing the *weighted residual function*

$$\int d^3x W^{(i)}(\mathbf{x}) \left(\Delta \Phi_{dc}^{(i)}(\mathbf{x}) \right) \quad (2.12)$$

the coefficients of the shape function can be found on each finite element [17]. The accuracy hence depends on the size of the finite elements as well as the functional form of the shape function. Finding suitable settings requires experience and is crucial for both precision and computational time [13].

2.2.2 Boundary Element Method

The finite element method is very versatile and can be used to solve any physical problem governed by PDEs. In the special case of finding an electrostatic potential generated by the trap electrodes there is, however, a much simpler solution: if the charge distribution $\rho(\mathbf{x})$ on the electrodes is known, the potential is given by the well-known formula [18]

$$\Phi_{dc}(\mathbf{x}) = \frac{1}{4\pi\epsilon_0} \int d^3x' \frac{\rho(\mathbf{x}')}{|\mathbf{x} - \mathbf{x}'|} \quad (2.13)$$

This idea is implemented in the BEM algorithm. Initially, only the surface of the electrode is meshed by a triangular grid and the charge on each mesh element is calculated. Next, equation (2.13) is written as a discrete sum over the mesh elements and the potential is calculated [13].

Since the algorithm is only evaluating two-dimensional surfaces instead of the whole three-dimensional space, BEM is potentially much faster than FEM. The downside of BEM is that only the potential can be calculated. FEM on the other hand also allows for studying of additional physical properties such as for example mechanical strain in the electrode structure [13].

2.2.3 Benchmarking of FEM and BEM

As shown for example in [13] and [20], BEM is superior to FEM in both precision and computational speed at the calculation of static electric potentials. Therefore, in our group an implementation of the BEM algorithm using the *fast multipole method* (see e.g. [21]) developed by R. Reichle and co-workers at NIST is used for trap simulation.

At the same time, COMSOL Multiphysics[®] [22], a commercial FEM solver is available.

Since commercial products are highly optimized and the benchmark in [20] dates back to 1999, the two solvers at hand were compared with analytically solvable problems to benchmark their precision.

Plate Capacitor The first electrode configuration that was tested was a large parallel plate capacitor oriented along the $\hat{\mathbf{z}}$ axis. When the potential difference between the two plates is V , the electric field and potential in between the plates are given by the well-known formulas

$$\mathbf{E}(\mathbf{x}) = \frac{V}{d} \hat{\mathbf{z}} \quad (2.14)$$

$$\Phi(\mathbf{x}) = -\frac{V}{d} z \quad (2.15)$$

where $d \ll \sqrt{A}$ is the separation of the two plates and A is their surface area.

The potential and electric field of a capacitor with a plate spacing of 10 mm were evaluated with both the BEM and FEM algorithm on a three-dimensional grid with a side length of 10 mm, centred at the origin. The results of this simulation are summarized in Table 2.1.

The *root-mean-square* (RMS) error of both potential and field obtained by the FEM algorithm are below 10^{-16} for all sizes of the mesh elements tested. BEM on the other hand showed an error of $\sim 0.4\%$ for the potential on a grid centred around the origin of the capacitor. By decreasing the size of the mesh elements the error was slightly decreased at the expense of a much longer simulation time.

| | $V_{RMS} [\%]$ | $ \mathbf{E} _{RMS} [\%]$ | time [min] |
|-----|----------------|---------------------------|------------|
| BEM | 0.44 / 0.38 | 0.08 / 0.09 | 1.0 / 8.4 |
| FEM | $< 10^{-16}$ | $< 10^{-16}$ | 1.0 |

Table 2.1: RMS value of the relative errors of the electric potential and field in a box with a side-length of 10 mm centred at the origin. The size of the mesh elements was 9.5 mm (5.1 mm for the second values in the BEM simulation).

The relative error of the electric field for BEM is plotted in Figure 2.2, showing that the electric field error (and the potential error as well) close to the boundary of the electrodes is larger than further away. This is due to the meshing of the surface which is not fine enough as mentioned in [13].

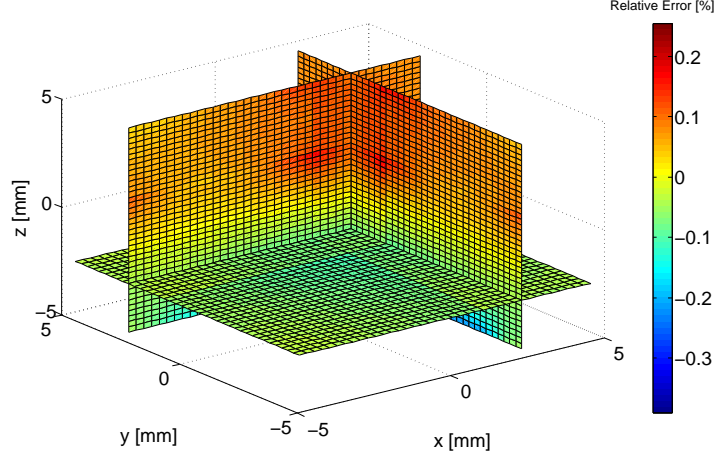


Figure 2.2: Relative error of the electric field simulated in BEM. The distance between the two plates of the capacitor aligned along the $\hat{\mathbf{z}}$ axis was 10 mm.

Charged Sphere Next, the potential and electric field of a sphere with radius $R = 1$ mm and charge¹ q , which are given by

$$\Phi(\mathbf{x}) = \frac{1}{4\pi\epsilon_0} \frac{q}{r} \quad (2.16)$$

$$\mathbf{E}(\mathbf{x}) = -\frac{1}{4\pi\epsilon_0} \frac{q}{r^2} \quad (2.17)$$

were numerically calculated. This problem is much more challenging than the plate capacitor because a curved surface has to be meshed.

The potential and the electric field were evaluated on a three-dimensional grid around the sphere, yielding the results presented in Table 2.2. Again, FEM performed better, i.e. giving more precise results in less time. Furthermore, the BEM results showed an overall offset (c.f. Figure 2.3), only slowly decreasing with a finer mesh.

The FEM results on the other hand showed discontinuities, especially in the electric field. For this reason the RMS error did not decrease when increasing the number of mesh elements. The problem is related to the choice of the shape function introduced previously. For the benchmarks presented so far, a quadratic shape function was used for calculating the potential. This is an appropriate choice in the case of the linear potential of a capacitor but not for the potential generated by the sphere simulated here. By increasing the polynomial degree of the shape function, the result can be improved.

| | V_{RMS} [%] | $ \mathbf{E} _{RMS}$ [%] | time [s] |
|-----|---------------|--------------------------|----------|
| BEM | 3.6 / 1.2 | 3.6 / 1.3 | 19 / 55 |
| FEM | 0.1 / 0.1 | 0.3 / 0.3 | 38 / 44 |

Table 2.2: RMS value of the relative errors of the electric potential and field in a box with a side length of 100 mm centred at the origin. The size of the mesh elements was set to be at most 2.5 mm / 0.5 mm.

¹The charge q on the sphere for a given potential V can be calculated from the condition that the potential on the surface must be V , i.e. $V = q/(4\pi\epsilon_0 R)$.

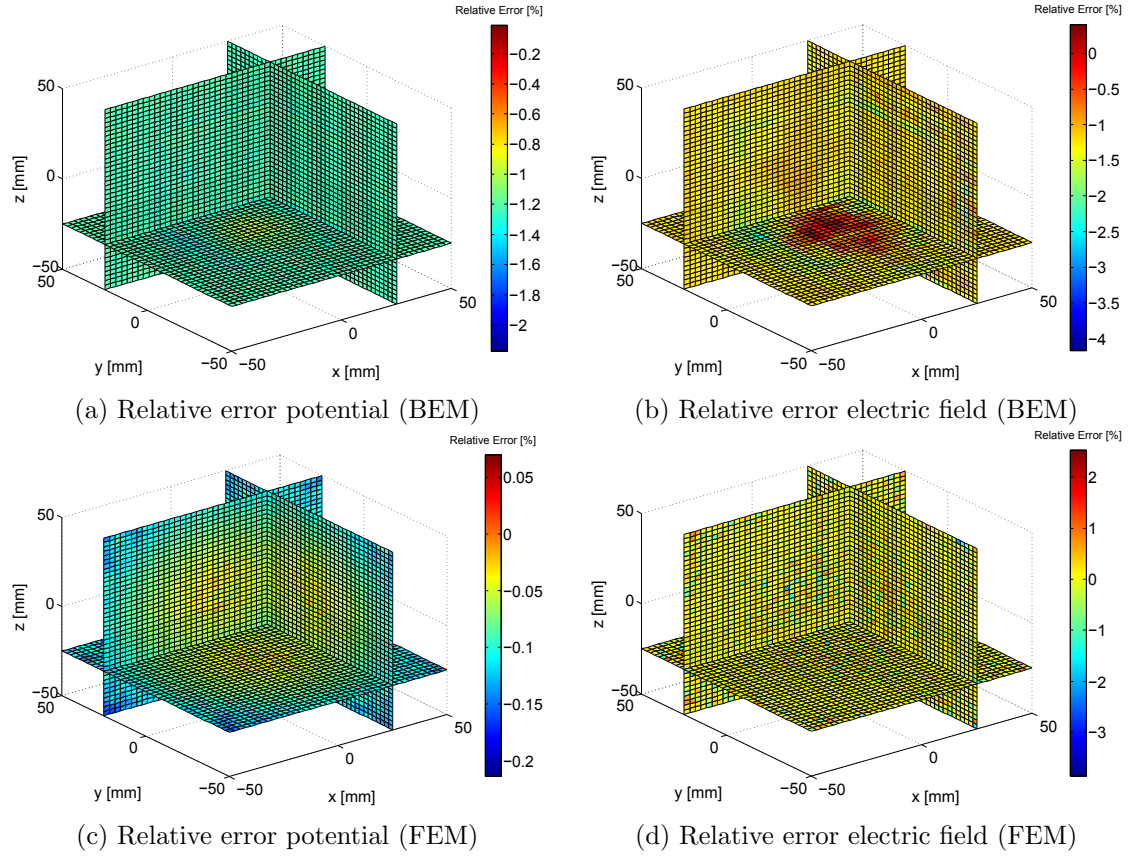


Figure 2.3: Relative errors for BEM and FEM. The FEM results are closer to the analytic solution but are not as continuous as the BEM results

Conclusions Both benchmarks showed that COMSOL is at the moment the better choice for trap simulation. Its precision and computational speed are unmatched by the implementation of BEM used at the moment. Furthermore, the meshing algorithm is better optimized such that the simulation of curved surfaces yields more accurate results. This most likely also explain the discrepancy of $\sim 1\%$ between the results obtained by BEM and the analytical solution for both potential and electric field.

The BEM implementation used for this benchmark was not optimized for modern computer systems, i.e. no multi-core CPUs were supported and the memory was limited to ~ 2 GB. COMSOL on the other hand can even be run on cluster systems, compensating algorithmic disadvantages with sheer computational power.

The results obtained with COMSOL also showed that it is very important to choose the appropriate functional form of the shape function in FEM simulations. In practice, a quartic function was found to be the best option for the simulation of rf ion traps where the potential cannot be approximated precisely enough by the quadratic function used by default.

3 Electro-Optical Trap Simulation

Section 2.2 described how charged particles can be trapped by radio-frequency fields utilizing their naturally strong interaction. Another technique, mainly used for trapping neutral particles, is the dipole trap [9], forming an optical lattice. It relies on the dipole interaction between the electro-magnetic field of light and the atomic dipole of an atom.

In the following a short introduction to dipole trapping is given. Then, a hybrid trap geometry is presented which combines a static electric potential and a dipole trap, able to trap ions, but potentially neutral atoms at the same time as well.

3.1 The Optical Dipole Trap

To date, most experiments with trapped ions are performed in rf traps as described in the previous chapter. More recently, experiments have been conducted in which an ion trapped in a Paul trap was sympathetically cooled by a cold bath of bosonic atoms [23]. It was shown that the micromotion induced by the rf drive limited the minimum temperature of the ion to ~ 0.5 mK, which is one order of magnitude larger than what is needed to conduct quantum information experiments [16].

For these reasons, ion traps have been proposed which confine the ion in an optical lattice, as it is already practised in cold atom experiments [9]. Such traps do not suffer from heating due to micromotion, but have the downside of a much shallower trapping potential, making loading more challenging.

First proof-of-principle experiments with single ions have been performed in focused beam [6] and counter-propagating beam [7] close-to-resonance dipole traps as well as far detuned traps [8]. In this thesis however, a potential generated by the far detuned mode of a build-up cavity was studied which allows for a larger spot size and therefore possibly ion confinements in three-dimensional lattices.

Additionally, dipole traps allow for simultaneous trapping of charged and neutral particles which is of particular interest in the simulation of quantum many-body systems and cold-chemistry experiments [6].

Theory of Optical Trapping in a Far Detuned Field In optical dipole traps, a laser beam detuned far from any transition is used to trap a particle just by its dipole interaction with the field. Since the laser is far detuned, optical excitation of the particle and hence transfer of momentum is very low and the interaction can be treated perturbatively [9]. The dipole interaction leads to an AC Stark shift of the energy levels which is modulated by the intensity of the laser [9]. Having a Gaussian beam profile thereby creates regions where the energy of a certain atomic state is lower, hence providing a confining trap for the particle. This is schematically sketched in Figure 3.1 where the strength of the AC stark shift is plotted as a function of distance from the centre of the beam.

The formal derivation is carried out in [9], yielding for a certain level i a potential of the form

$$\Phi_D^{(i)}(\mathbf{x}) \approx \sum_j \frac{3\pi c^2}{2\omega_{ij}^3} \frac{\Gamma_{ij}}{\Delta_{ij}} I(\mathbf{x}) \quad (3.1)$$

where the sum is taken over all energy levels that have allowed transitions to level i . Here, $I(\mathbf{x})$ is the intensity of the laser beam, Δ_{ij} is the detuning of the laser with respect to the atomic transition between the energy levels i and j , $\omega_{ij} = \omega_j - \omega_i$ is the energy difference between the levels and Γ_{ij} the decay rate of the upper state.

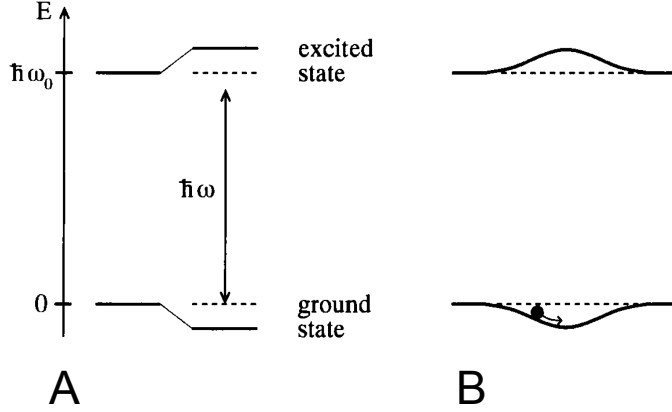


Figure 3.1: (A) AC Stark shift of the ground and excited state of a two-level system. (B) AC Stark shift as a function of position in a Gaussian beam, leading to a confining potential for the ground state. Images taken from [9].

Using the Gaussian mode of an optical cavity, as will be discussed in the following, is advantageous compared to using a single beam [6] or the standing wave pattern of two counter-propagating beams [7]. The power build-up in a cavity leads to a factor-of-four deeper potential than in a focused beam trap [9] and therefore allows for looser focusing or further detuning from the transition.

As shown in [9] the standing wave pattern of a mode inside a cavity leads to a fully confining optical lattice and the intensity of the beam when the cavity is aligned along the $\hat{\mathbf{z}}$ axis is given by [10]

$$I(r, z) = \frac{8P}{\pi w^2(z)} \cos^2(kz) \exp\left(-\frac{2r^2}{w^2(z)}\right) \quad (3.2)$$

with the usual definitions² of beam waist w_0 , beam width $w(z)$, Rayleigh range z_0 and average power P .

Therefore, the dipole potential acting on particles inside the mode of an optical cavity is given by

$$\begin{aligned} \Phi_D^{(i)}(r, z) &\approx \sum_j \frac{12Pc^2}{w^2(z)w_{ij}^3} \frac{\Gamma_{ij}}{\Delta_{ij}} \cos^2(kz) \exp\left(-\frac{2r^2}{w^2(z)}\right) \\ &\equiv -\frac{U_0^{(i)}}{\eta^2(z)} \cos^2(kz) \exp\left(-\frac{2r^2}{w^2(z)}\right) \end{aligned} \quad (3.3)$$

where $\eta(z) = w(z)/w_0$ and the AC Stark shift $U_0^{(i)}$ determines the maximum potential depth for a certain energy level i and a given optical lattice.

3.2 Geometry of the Electro-Optical Trap

To my knowledge, among all the published experiments performed with ions in an optical lattice so far, only single ion were trapped [6], [7], [8]. Interesting physical systems however involve lattices filled with multiple ions, for example for scaling the ion quantum computer in two dimensions or the simulation of quantum many-body models. Such

²see e.g. B.E.A. Saleh and M.C. Teich, *Fundamentals of Photonics*. 2nd edition (John Wiley & Sons, Hoboken, 2007), p.77.

systems have so far only been studied in rf-optical hybrid traps (e.g. [24]) which are limited by the micromotion as outlined before.

Therefore, in this section a new trap design is presented, utilizing the confinement of a dc electric field in two dimensions and the optical lattice in the third. Such a trap geometry does not suffer from rf heating and additionally allows scaling in two dimensions as well as simultaneous trapping of neutral and charged particles.

Besides the linear Paul trap presented in Section 2, there is a wide range of possible geometries producing similar potentials. One design commonly used in single-ion spectroscopy is the cylindrical trap [25]. The cylinders defining the trap are easier to machine and to align than a Paul trap [26]. Furthermore, the trap provides good optical access to the ion due to the large aperture of the cylinders. By applying a radio-frequency signal to the middle ring electrode (see Figure 3.2a), a quadrupole-like potential can be generated in the centre of the trap [26]. Additionally, the endcap electrodes can be used to add a static offset to the potential.

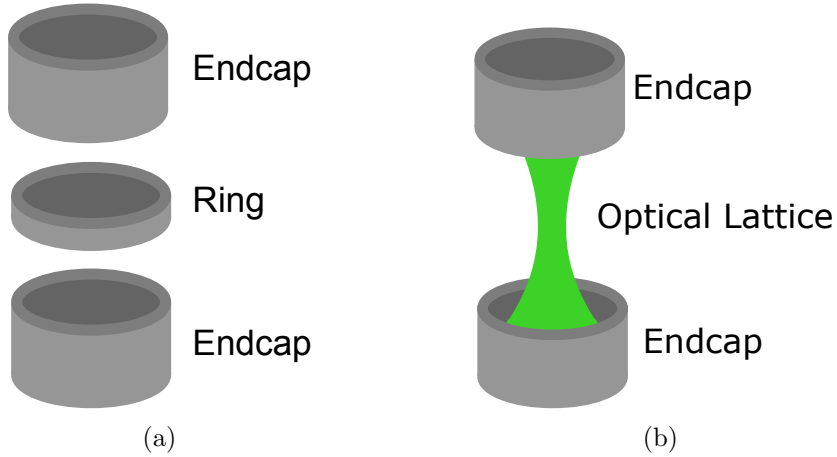


Figure 3.2: (a) Sketch of a cylindrical ion trap following [26]. The radio-frequency voltage is applied to the ring electrode and the endcaps can be used to apply a constant potential offset. (b) The hybrid electro-optical trap. The ring electrode is replaced with an optical lattice generated by a Gaussian cavity mode.

The optical trap is aligned along the cylinder axis as depicted in Figure 3.2b. This is the only geometry in which both electric and optical potential can be used for trapping ions. Due to the symmetry of the cylinder trap, the radial potential direction is always completely confining or anti-confining. Therefore, if the dipole trap is oriented in radial direction, one of the anti-confining axes of the electric potential will coincide with one of the weakly confining axes of the dipole potential, leading to a very unstable trap.

To gain perpendicular access to the trap centre with control and cooling beams, the ring electrode has to be either removed or replaced by a segmented ring. The latter would be advantageous in the sense that ions could be trapped in a radio-frequency trap with a deeper potential and then adiabatically transferred to the hybrid trap as shown for example in [6]. The downside of this geometry is that the electrode loses its cylindrical symmetry and hence the quadrupole-like potential. For correction, additional electrodes have to be used for compensation [26], making the trap more complex and less accessible with further diagonal lasers, e.g. for Doppler cooling.

3.3 Electro-Optical Trap Simulation

This section describes the techniques used to simulate the dynamics of charged particles in an electro-optical trap. The simulation solves the classical equation of motion of charged particles in the presence of an electrical as well as an optical potential. Furthermore, the Coulomb interaction between the particles and the damping due to a Doppler-cooling laser beam are considered. Since the cooling term introduces a damping, certain sets of parameters will lead to an equilibrium state of the system. For solving the equation of motion, a modified version of the Verlet algorithm, typically used in molecular dynamics simulations, is used.

3.3.1 Numerical Solving of Equations of Motion: The Verlet Algorithm

The simulation of the dynamics of interacting N -body systems is a problem often encountered in numerical physics. A classical physical system can be described by a set of differential equations (equations of motion) which are derived from the net force F_i acting on each particle i

$$m_i \frac{d^2 x_i}{dt^2} = F_i \quad (3.4)$$

where x_i is the position coordinate of particle i and m_i is its mass.

Many different algorithms for solving differential equations exist, for example the important class of Runge-Kutta methods. However, most of these integrators are not well suited for solving physical systems since quantities like total energy and momentum are not long-time conserved.

This is illustrated in Figure 3.3 where the Runge-Kutta method is used to solve the Kepler problem. For large numbers of time steps the trajectory diverges from the analytical solution. On the other hand, the solution obtained by the so-called Verlet method³ is oscillating about the correct trajectory and is not diverging. It turns out that the Verlet algorithm is symmetric with respect to changing the direction of time and therefore conserves the total energy in periodic problems [27].

A further advantage of the Verlet method is that it is explicit, i.e. the solution at time t_{n+1} can be explicitly calculated from the solutions at previous time steps. In contrast, in each step of an implicit method (for example a Runge-Kutta solver) the solution of a nonlinear equation must be found.

For these reasons, the Verlet algorithm is the preferred method for simulating physical systems of any size, ranging from finding the trajectories of planets to the dynamics of single atoms [29].

However, the standard Verlet method requires a conservative force, which implies that the force depends solely on the position of the particles, i.e. $F_i = F_i(x_1, \dots, x_N)$. In order to solve an equation of motion of the form

$$m_i \frac{d^2 x}{dt^2} = F_i(x_1, \dots, x_N) - \gamma v_i \quad (3.5)$$

with a velocity-dependent friction term γv_i , the Verlet method can be extended to the

³This method is also known in slightly different forms as *Störmer*, *Störmer-Verlet*, *Encke* or *leapfrog method* [29].

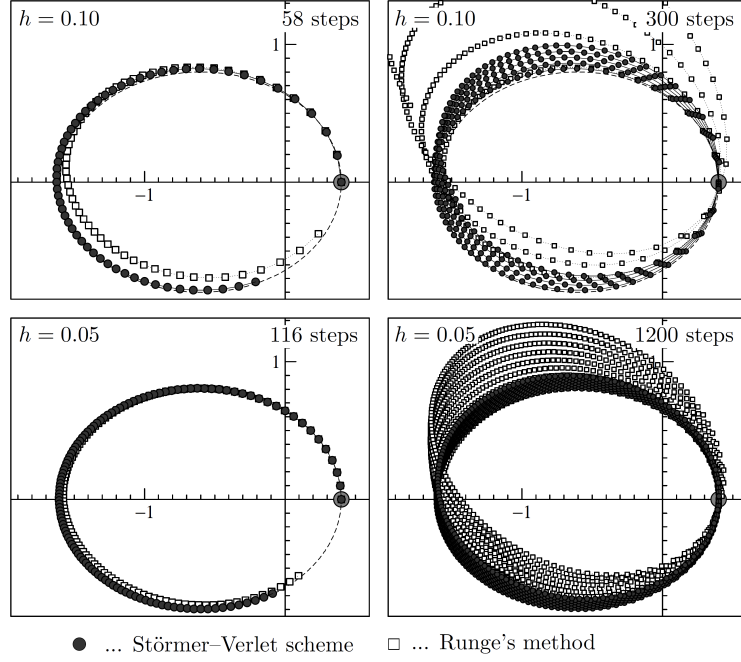


Figure 3.3: Comparison of the Verlet and the Runge-Kutta method for the Kepler problem. The dashed line is the exact solution. Image taken from [29].

following algorithm [28]

$$x_i^{(n+1)} - x_i^{(n)} = b_i \Delta_t \left(v_i^{(n)} + \frac{\Delta_t}{2m} F_i^{(n)} \right) \quad (3.6)$$

$$v_i^{(n+1)} - v_i^{(n)} = \frac{\Delta_t}{2m} \left(F_i^{(n)} + F_i^{(n+1)} \right) - \frac{\gamma}{m} \left(x_i^{(n+1)} - x_i^{(n)} \right) \quad (3.7)$$

where $F_i^{(n)} = F_i^{(n)}(x_1, \dots, x_N)$ is the position-dependent force term at time step n . The constant b_i is given by

$$b_i = \frac{1}{1 + \gamma \Delta_t / (2m_i)} \quad (3.8)$$

for a given time step Δ_t , damping coefficient γ and mass m_i .

This algorithm was used throughout this thesis for simulating the equation of motion of ions trapped in an electro-optical hybrid trap as discussed in the next section.

Time Step Size Due to the very small mass of the ions on the order of $\sim 10^{-26}$ kg, great care must be taken when choosing the size of the time steps Δ_t .

If the time steps are too fine, finding the equilibrium configuration of the system becomes impractical since the computational time scales as Δ_t^{-1} .

On the other hand, choosing too-large time steps violates the underlying assumptions of the algorithm. The terms mostly affected are those scaling as Δ_t/m which occur in the calculation of $\Delta v_i^{(n+1)} = v_i^{(n+1)} - v_i^{(n)}$. Hence, a time step which is too coarse will violate the assumption $\Delta v_i^{(n+1)} \ll v_i^{(n+1)}$, implicitly required when approximating the integral

$$\int_{t_n}^{t_{n+1}} dt v_i(t) \approx \frac{\Delta_t}{2} \left(v_i^{(n)} + v_i^{(n+1)} \right) \quad (3.9)$$

using the trapezoidal rule (see equation (15) in [28]).

From (3.7), a simple criterion for finding an appropriate step size can be derived by requiring that both terms are small, i.e.

$$\frac{\Delta_t}{2m_i} \left(F_i^{(n)} + F_i^{(n+1)} \right) \leq \frac{\Delta_t}{m_i} \max |F_i(t)| \ll v_i^{(n+1)} \quad (3.10)$$

$$\frac{\gamma}{m_i} \left(x_i^{(n+1)} - x_i^{(n)} \right) \leq \gamma b_i \left(\frac{\Delta_t}{m_i} \max |v_i(t)| + \frac{\Delta_t^2}{2m_i^2} \max |F_i(t)| \right) \ll v_i^{(n+1)} \quad (3.11)$$

Since

$$\gamma b_i \frac{\Delta_t}{m_i} = \frac{m_i}{m_i(1 + \gamma \Delta_t m_i)} = 1 + \mathcal{O}(\gamma \Delta_t m_i) \quad (3.12)$$

the condition for the maximal allowed step size can be reduced to

$$\Delta_t \ll \frac{m_i}{\max |F_i|} \quad (3.13)$$

which results in $\Delta_t \approx 1 \text{ ns}$ for $\max |F_i(t)| \sim 10^{-18} \text{ N}$.

3.3.2 The Equation of Motion

The net force acting on particle i in an ensemble of N charged particles is given by the sum of Lorenz and Coulomb forces as well as the force due to the dipole trapping potential and the Doppler cooling beams. Formally

$$\begin{aligned} \mathbf{F}_i^{\text{tot}} &= \mathbf{F}_L(\mathbf{x}_i) + \sum_{i \neq j} \mathbf{F}_C(\mathbf{x}_i, \mathbf{x}_j) + \mathbf{F}_D(\mathbf{x}_i) + \mathbf{F}_{DC}(\mathbf{v}_i) \\ &\equiv \mathbf{F}_i(\mathbf{x}_1, \dots, \mathbf{x}_N) + \mathbf{F}_{DC}(\mathbf{v}_i) \end{aligned} \quad (3.14)$$

where \mathbf{x}_i is the position of particle i and \mathbf{v}_i is its velocity. All except the force simulating the Doppler cooling are solely position dependent and thus collected in the term $\mathbf{F}_i(\mathbf{x}_1, \dots, \mathbf{x}_N)$ in resemblance to equation (3.5).

Lorentz Force A particle with charge q experiences a Lorentz force

$$\mathbf{F}_L(\mathbf{x}, \mathbf{v}) = q\mathbf{E} = -q\nabla\Phi(\mathbf{x}) \quad (3.15)$$

in an electrical field \mathbf{E} .

The methods described in Section 2 can be used to numerically calculate the potential generated by arbitrary electrode configurations. However, the simulation yields only values for the potential on a discretized grid in space. Hence, an approximation for points in between must be found.

In the case of the hybrid-trap, the dc potential in the xy plane can be well described by the quadratic, radially symmetric function

$$\Phi(x, y) \approx P_r(x^2 + y^2) + P_a \quad (3.16)$$

as shown in Figure 3.4c.

For each axial position z_i on the discrete grid, the potential can be fitted by $\Phi(x, y)$ and the coefficients $P_r(z_i)$ and $P_a(z_i)$ can be found. This is shown in Figures 3.4a and 3.4b implying the following z dependence of the parameters P_r and P_a

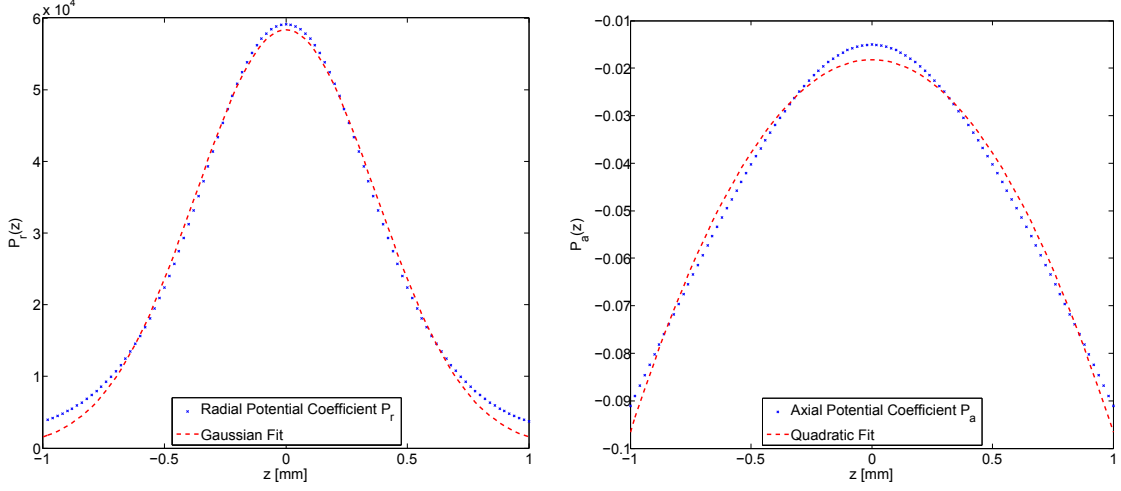
$$P_r(z) = r_1 e^{-\left(\frac{z-r_2}{r_3}\right)^2} \quad (3.17)$$

$$P_a(z) = a_1 z^2 + a_2 \quad (3.18)$$

This choice leads to a total potential

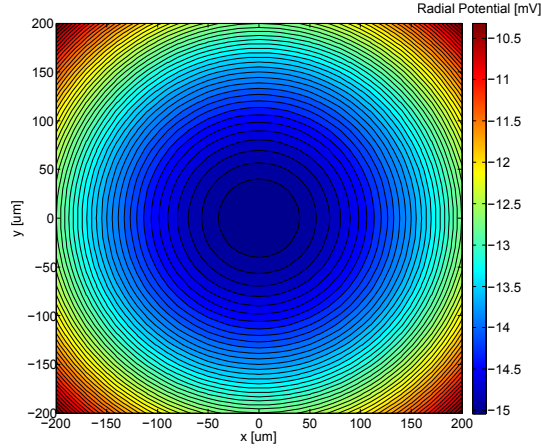
$$\Phi(x, y, z) = r_1 e^{-\left(\frac{z-r_2}{r_3}\right)^2} (x^2 + y^2) + a_1 z^2 + a_2 \quad (3.19)$$

In cases where the potential is too complicated to fit, a feasible approach would be to simulate the potential on a very fine grid and then use the nearest grid point as an approximation. This method was implemented as well but turned out to slow down the simulation considerably and hence not used.



(a) The coefficient P_r determined by a least square fit for different axial positions. The z dependence can be fitted with a Gaussian (red dashed line).

(b) The coefficient P_a also determined by a least square fit for different axial positions and fitted with a anti-confining quadratic potential.



(c) The dc potential $\Phi(x, y)$ at $z = 0$ when a volage of -500 mV is applied to the endcaps of the hybrid trap.

Figure 3.4

Optical Dipole Force The potential generated by an optical lattice is given by equation (3.3). In order to get a fully trapping potential with maximal depth, the laser was aligned along the anti-confining axis of the electrical potential, i.e. along the cylinder axis.

The dipole force acting on state i generated by this optical lattice is then given by

$$\begin{aligned}\mathbf{F}_D^{(i)}(\mathbf{x}) &= \nabla \Phi_D(\mathbf{x}) \\ &= \frac{2U_0^{(i)} \cos(kz)}{w^2(z)} \exp\left(-\frac{2r^2}{w^2(z)}\right) \begin{pmatrix} 2x \cos(kz) \\ 2y \cos(kz) \\ -\frac{2z \cos(kz)}{z_0^2 \eta(z)} + \frac{w_0^2 z \cos(kz)}{z_0^2 \eta(z)} + kw_0 w(z) \sin(kz) \end{pmatrix}\end{aligned}\quad (3.20)$$

Coulomb Force The Coulomb force acting on charge i in an ensemble of N particles at positions \mathbf{r}_j and with charges q_j is given by

$$\mathbf{F}_C^{(i)} = \sum_{j \neq i}^N \frac{1}{4\pi\epsilon_0} \frac{q_i q_j}{|\mathbf{r}_j - \mathbf{r}_i|^2} \hat{\mathbf{r}}_{ji} = \sum_{j \neq i}^N \frac{1}{4\pi\epsilon_0} \frac{q_i q_j}{|\mathbf{r}_j - \mathbf{r}_i|^3} (\mathbf{r}_j - \mathbf{r}_i). \quad (3.21)$$

In each time step, the distance between all particles must be calculated which makes the Coulomb force the most time-consuming calculation.

Doppler Cooling A widely used method for cooling ions to a temperature in the millikelvin range is Doppler cooling [30]. It relies on the Doppler shift of the frequency of photons seen by an ion with velocity \mathbf{v} . In the reference frame of the ion, the frequency of a counter-propagating photon is increased, ideally shifted to the transition frequency of the ion to a fast decaying (dipole-allowed) energy level. The photon emitted subsequently due to spontaneous emission will have little correlation⁴ with the direction of the absorbed photon and since energy and momentum must be conserved, the ion effectively loses energy when scattering many photons.

The force due to the cooling laser acting on the ion is given by the photon momentum $\hbar\mathbf{k}$ ($|\mathbf{k}| = 2\pi/\lambda$ is the wavenumber of the photon) times the absorption rate R [31]. From the steady-state condition of the optical Bloch equations for a two-level system the scattering rate

$$R = \Gamma \frac{\Omega^2/4}{\delta^2 + \Omega^2/2 + \Gamma^2/4} \quad (3.22)$$

can be derived [32]. Here, Γ is the decay rate of the upper level state, Ω is the Rabi frequency of the cooling laser and δ the detuning from the transition. Due to the Doppler effect the detuning $\delta = \delta_0 \pm \mathbf{k}\mathbf{v}$ is shifted according to the relative motion of the ion with respect to the cooling beam (positive sign for a counter-propagating beam).

Expanding the force in the velocity \mathbf{v} yields [32]

$$\begin{aligned}\mathbf{F}_{DC} &= \hbar\mathbf{k}\Gamma \frac{\Omega^2/4}{(\delta_0 - \mathbf{k}\mathbf{v})^2 + \Omega^2/2 + \Gamma^2/4} \\ &= \hbar\mathbf{k}\Gamma \frac{\Omega^2/4}{\delta_0^2 + \Omega^2/2 + \Gamma^2/4} + \frac{\hbar\mathbf{k}}{2} \underbrace{\frac{2s}{(1+s)^2}}_A \underbrace{\frac{\delta_0\Gamma}{\delta_0^2 + \Gamma^2/4}}_B \mathbf{k}\mathbf{v} + \mathcal{O}(\mathbf{v}^3) \\ &\approx \mathbf{F}_{DC,0} - \frac{\gamma}{2} \mathbf{v}\end{aligned}\quad (3.23)$$

⁴Since a dipole transition is used for cooling, the probability of emission along the dipole axis is lower than in the perpendicular direction. For the analysis performed here, the correction factor can, however, be neglected and the emission can be assumed to be isotropic.

where

$$s = \frac{\Omega^2/2}{\delta_0^2 + \Gamma^2/4} \quad (3.24)$$

The result from (3.23) is exactly of the form of a damping force with a damping rate $\gamma/2$ with an additional constant force in the direction of the cooling beam. This constant term can be cancelled out by retro-reflecting the cooling laser. The velocity dependent terms thereby do not cancel because the reflected beam is Doppler-shifted in the opposite direction.

The maximum damping can be found by simultaneously maximizing parts A and B in (3.23). From B the optimum detuning $\delta_0 = -\Gamma/2$ can be found. Plugging this result back into A yields the optimal Rabi frequency $\Omega = \Gamma$. Hence, for two counter-propagating beams

$$\mathbf{F}_{DC}^{\max} \approx -\frac{\hbar}{4}\mathbf{k}^2\mathbf{v} = -\frac{\pi\hbar}{2\lambda^2}\mathbf{v} \quad (3.25)$$

3.3.3 Magnesium in an Optical Lattice

As shown in [10], both ^{40}Ca and ^9Be which are currently used in our lab are not well suited for optical trapping because some levels used in the common qubit schemes are not confined in an optical lattice generated by a laser with a wavelength of $\lambda = 532\text{ nm}$. Out of the alkali earth elements often used in trapped ion quantum information experiments, ^{25}Mg is the best suited candidate for optical trapping because all relevant energy levels are confined [10].

Due to the residual magnetic moment of the nuclear spin of ^{25}Mg (as opposed to the more common ^{24}Mg) the energy eigenstates of the electronic system are split up in hyperfine levels, according to the total angular momentum operator $\hat{F} = \hat{I} + \hat{J}$ of the composite system of nuclear and electronic spin.

The qubit levels are chosen in the $F = 3$ (pseudo-spin state $|\downarrow\rangle$) and $F = 2$ ($|\uparrow\rangle$) manifold of the $3S_{1/2}$ ground state [33]. The splitting of the qubit levels is on the order of gigahertz and therefore the levels are either coupled by Raman-transitions [10] or microwave fields [33].

Depending on the strength of the magnetic field that is required to lift the degeneracy of the states, different first-order field-independent qubits can be identified [33].

For the simulations of magnesium ions in the electro-optical trap, presented in the next section, the qubit was defined as $|\downarrow\rangle = |F = 3, m_f = -2\rangle$ and $|\uparrow\rangle = |F = 2, m_f = -2\rangle$ as schematically depicted in Figure 3.5. This choice leads to an AC stark shift of the ground state of $U_0 = -3.33615 \times 10^{-25}\text{ J} \approx -k_B \times 24\text{ mK}$ [10] with the experimental parameters presented in Table 3.1a.

| | | | |
|-----------|-----------|------------------|--|
| λ | P_{avg} | w_0 | $\omega_z \approx 2\pi \times 7.69\text{ MHz}$ |
| 532 nm | 1 kW | 30 μm | $\omega_r \approx 2\pi \times 30.7\text{ kHz}$ |

(a) Parameters of the trapping laser used for the Simulation of ^{25}Mg in an optical lattice.

(b) Axial and radial trapping frequencies of the qubit ground state $|F = 3, m_f = -2\rangle$

Table 3.1: Simulation parameters.

The same parameters for the trapping laser were chosen as M. Marinelli designed the build-up cavity for, which will be presented in the next chapter. The reason for choosing a frequency doubled Nd:YAG laser with a wavelength of 1064 nm for generating the optical lattice is that such lasers are widely used in industry, hence very stable and powerful

commercial products exist. Additionally, the second-harmonic generation efficiency of a Nd:YAG laser is comparably large and efficiencies of $> 30\%$ can be achieved by single-passing a quasi-phasematched nonlinear crystal [11].

It would be also possible to use the fundamental harmonic of the Nd:YAG, but then higher intra-cavity powers are required due to the larger detuning Δ_{ij} . Therefore the chosen wavelength is a compromise between low laser power needed to create a deep-enough trapping potential, and effort required to generate the light.

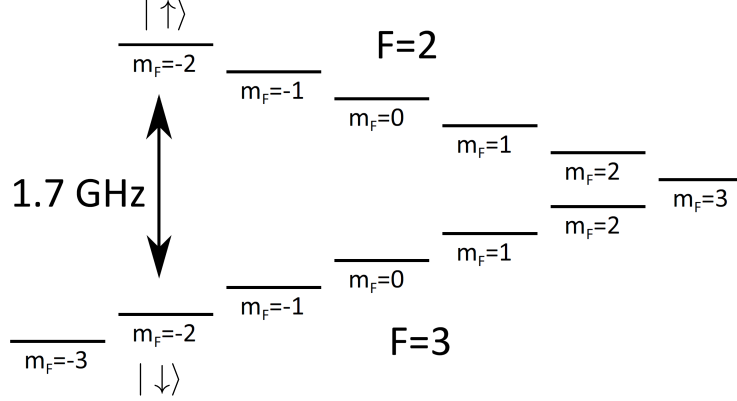


Figure 3.5: The qubit levels were chosen in the hyperfine manifold of the $3S_{1/2}$ ground state of ^{25}Mg . Image from [10].

3.3.4 Simulation Results

A drawing of the cylinder trap which was used for the simulation is shown in Figure 3.6. The aspect ratios of the cylinders

$$r_1 = 1.8r_0 \quad (3.26)$$

$$2z_0 = 1.12r_0 \quad (3.27)$$

were chosen in accordance with the optimal values reported in [25]. Here r_0 and r_1 denote the inner and outer radius of a cylinder, respectively and $2z_0$ is its height as depicted in Figure 3.6.

The exact dimensions of the trap must, however, be chosen with great care. On the one hand, the larger the electrode spacing d , the smaller the axial potential becomes. This is favourable because the repelling ions otherwise cannot be stopped by the optical lattice and are accelerated by the static electric field out of the trap. On the other hand, the radial potential must be made as large as possible, i.e. r_0 must be decreased. This is because the optical potential in radial direction is on the order of $\sim 10^{-22}$ N whereas the force exerted on the ions due to Coulomb interaction is initially on the order of $\sim 10^{-18} - 10^{-20}$ N. Hence, if the axial potential is too weak, the ions cannot be kept as well.

These considerations led to an inner cylinder radius of $r_0 = 3.5$ mm and a separation of $d = 10$ mm. The static electric potential produced by the cylinders was then simulated using the method described in Chapter 2 and used throughout all simulations presented in the following.

For the simulation a certain number of ions were “loaded” to the centre of the trap in a Coulomb-crystal like structure [30] and their evolution was studied for different initial spacings and electrode potential. One example of such a starting configuration is shown

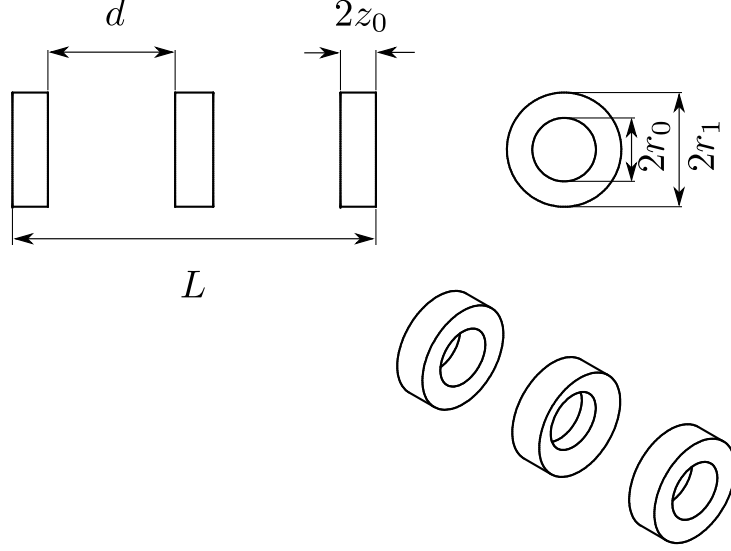


Figure 3.6: Drawing of the cylinder trap.

in Figure 3.7a. The distance r between individual ions was set to be between $5 - 10 \mu\text{m}$ by adding a random uncertainty factor to each initial position.

For the first simulations a static electric field was applied to the electrodes and the evolution in the hybrid trap was studied. Figure 3.7b shows a typical trajectory of an ion, showing that it was not trapped.

By careful analysis of the individual components of the force acting on each ion, two regimes were found

- The initial spacing of the ions was too small which resulted in an strong repulsion away from the trap centre. The optical potential slowed the ions down, but was not strong enough to stop them. At some point, the anti-confining electrical started to dominate over the optical potential, resulting in an unstoppable acceleration along the anti-confining axis.
- The initial spacing was too large. This resulted in a situation in which each ion found the nearest potential minimum of the optical lattice and no Coulomb interaction took place. Therefore, the final state of the trap was determined solely by the initial condition.

These observations led to the conclusion that the initial spacing of the ions must be made larger than $\sim 10 \mu\text{m}$ otherwise not a single ion can be kept in the trap. However, this regime is not very interesting to study, because only little interaction between the ions takes place and the result is very similar to the initial conditions.

In a second step the model was extended to a more realistic simulation. Instead of having a static electric potential which is anti-confining in one direction, the simulation started with a fully confining rf-potential. The strength of that potential was then slowly decreased while, at the same time, the dc potential was gradually turned on.

In this simulation, the ions were able to interact in the beginning without being kicked out of the trap and slowly arranging themselves in the potential. Then, when the confining axial potential was decreased, the ions adapted to the new potential landscape without being unstoppable accelerated.

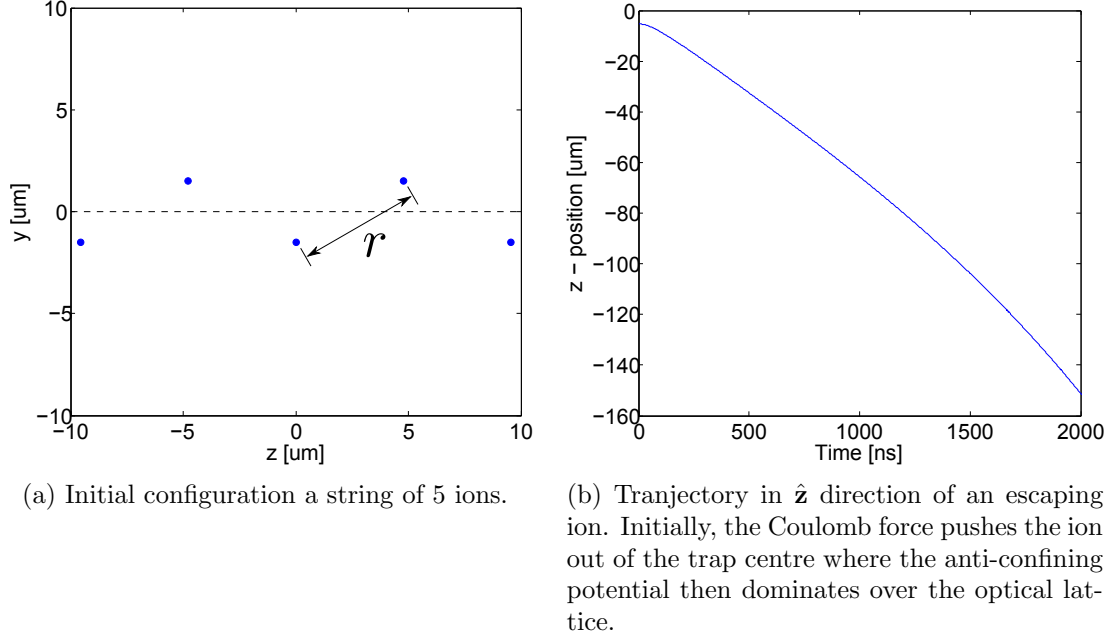


Figure 3.7

Indeed, when for example having a transition time of $\Delta\tau = 200 \mu\text{s}$, it was possible to store 8 ions in the trap as shown in Figure 3.8. The ions arranged radially in a ordered structure while the axial spacing was more disordered and also more stretched out.

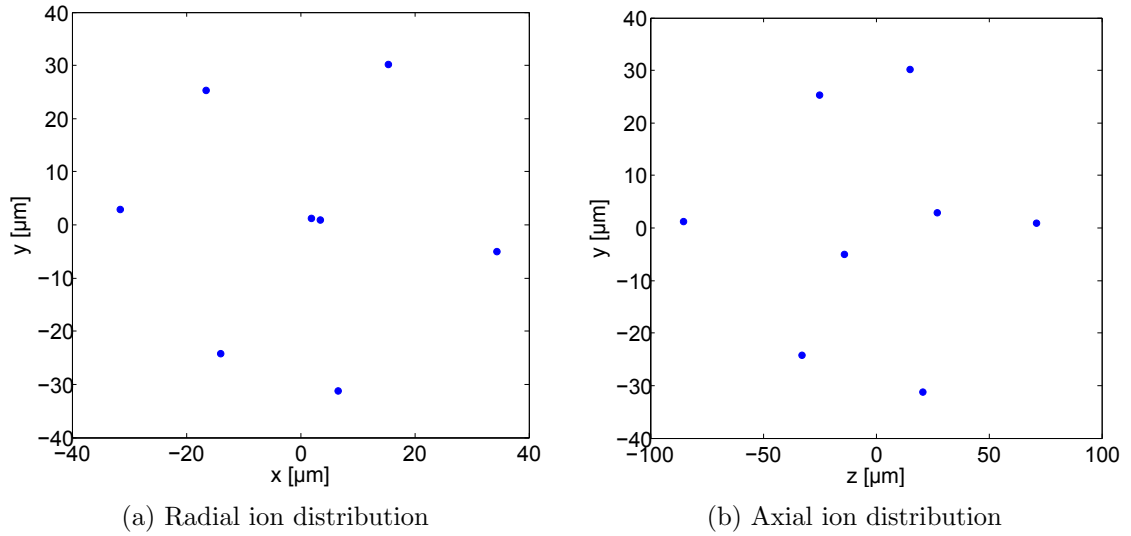


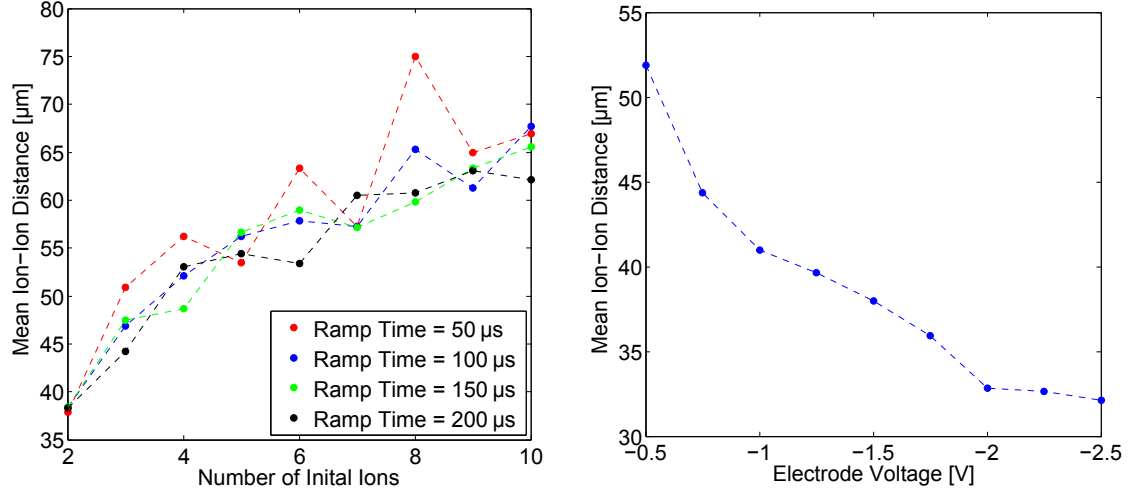
Figure 3.8: Final ion position for a simulation with 8 ions using a transition time of $\Delta\tau = 200 \mu\text{s}$ and a static potential of $V = -2.5 \text{ V}$.

The maximum number of ions that could be trapped was limited by the axial extend of the outermost ions and the strength of the axial potential. The larger the distance of the ions to the trap centre, the larger the potential force and hence, at some point the optical lattice was no longer able to compensate for the axial anti-confinement.

Figure 3.9a shows the mean ion-ion distance for different transition times $\Delta\tau$ as a function of initial number of ions in the trap. For a fast ramping time the probability of

loosing ions as well as the spacing between the ions was larger. For longer ramp times the average separation became independent of $\Delta\tau$ and the probability of loosing an ion is also decreased.

Finally, Figure 3.9b shows the mean ion-ion distance for an initial configuration of 5 ions and an electrode voltage between -0.5 V and -2.5 V. As expected, the spacing can be decreased by increasing the static electric potential.



(a) Final mean ion-ion spacing for a static potential of -500 mV for different transition times $\Delta\tau$ and 2–10 ions initially loaded. The kinks can be explained by ions that were lost during the transition.

(b) Final mean ion-ion spacing for 5 ions depending on the trap electrode voltage.

Figure 3.9

4 Optical Setup

In the following chapter the optical setup is described⁵. The setup is depicted in Figure 4.1 and can be split into two parts: the frequency doubling stage (upper part of Figure 4.1) following closely the scheme in [11], and the high-finesse cavity with its incoupling optics (lower part).

First, an introduction to second harmonic generation and quasi phase matching in periodically poled crystals is given. This section is followed by a description of the experimental setup used for frequency doubling of a diode pumped Nd:YAG laser. The results are then compared with the values reported in [11], where a similar setup was used.

The third section covers the *high finesse* (hf) cavity designed for optical trapping as described in Section 3.1. First, a method for stabilizing a laser to an optical cavity is discussed, which was used in the experimental setup described in the following part. The chapter is concluded with the experimental results found when trying to lock the frequency-doubled laser to the build up cavity.

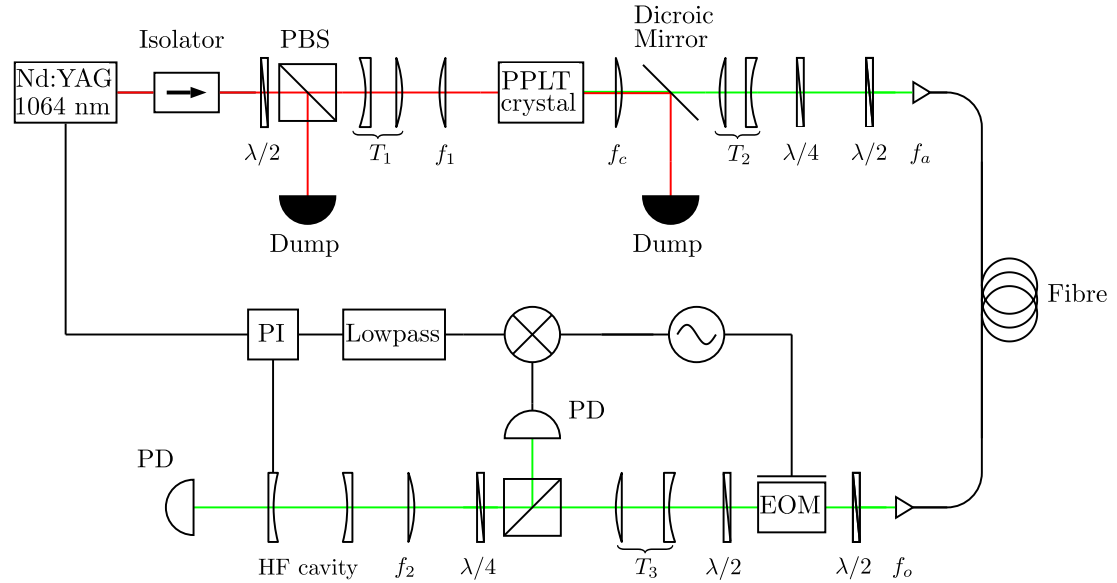


Figure 4.1: Optical Setup. The red line indicates the beam path of the fundamental harmonic at $\lambda_p = 1064\text{ nm}$ and the green line the path of the second harmonic at $\lambda_s = 532\text{ nm}$.

4.1 Second Harmonic Generation

This section gives an introduction to the theory of (type-I) second harmonic generation, showing its limitations due to phase mismatch of the fundamental and the second harmonic wave. In the second part, a technique called quasi phase-matching is discussed, strongly relaxing the conditions imposed by phase-matching. In the last part, the experimental setup used in this thesis for quasi-phase-matched second harmonic generation of green light with a wavelength of 532 nm is presented and the results obtained are compared with those found in literature with the similar setup.

⁵A complete list of all lenses used in the setup can be found in Appendix A.1.

4.1.1 Theory of Second Harmonic Generation

The wave equation in a dielectric medium with polarization $\mathcal{P}(E) = \epsilon_0\chi E + \mathcal{P}_{NL}(E)$ is [34]

$$\nabla^2 E - \frac{1}{c^2} \frac{\partial^2 E}{\partial t^2} = -S \quad (4.1)$$

where $c = c_0/n$ is the speed of light in the medium, $n = \sqrt{1 + \chi}$ is the refractive index and the source term S is defined as

$$S = -\mu_0 \frac{\partial^2 \mathcal{P}_{NL}(E)}{\partial t^2} \quad (4.2)$$

The nonlinear term \mathcal{P}_{NL} can be found by Taylor expansion of the polarization \mathcal{P} . For SHG, only the first-order term

$$\mathcal{P}_{NL} = 2dE^2 \quad (4.3)$$

is of interest. Here d is called the nonlinear second order coefficient of the dielectric medium.

When the incident electric field is a plane wave, the field at a certain point z_0 in the crystal is $E(t) = E_0 \cos(kz_0 - \omega t)$. Without loss of generality z_0 can be set to zero and the nonlinear polarization is given by

$$\begin{aligned} \mathcal{P}_{NL}(E) &= 2dE_0^2 \cos^2(\omega t) \\ &= dE_0^2 + dE_0^2 \cos(2\omega t) \end{aligned} \quad (4.4)$$

where the well-known trigonometric identity $\cos^2(x) = \frac{1}{2}(1 + \cos(2x))$ was used. Substituting this result back into equation 4.2 leads to a source term oscillating at 2ω , generating a second field at twice the frequency of the incoming wave. This process is called *second harmonic generation* (SHG).

Since energy must be conserved, two photons with frequency ω are needed to create one photon at 2ω . Additionally, momentum must be conserved, yielding the so-called *phase matching condition*

$$\mathbf{k}_{p,1} + \mathbf{k}_{p,2} = \mathbf{k}_s \quad (4.5)$$

where \mathbf{k} is the wavenumber in the medium with $|\mathbf{k}| = \omega n$. Here p denotes an incoming *pump* photon and s the *signal* photon.

In the case of type-I SHG, i.e. only one pump beam with a certain polarization, the phase matching condition simplifies to

$$2\omega_p n_p = \omega_s n_s = 2\omega_p n_s \Rightarrow n_p = n_s \quad (4.6)$$

Due to the wavelength dependence of the refractive index, birefringent materials have to be used under well-defined angles to achieve phase matching. However, the conversion efficiency is determined by d which is not the same along different crystal axes, hence only very few frequencies can be efficiently frequency-doubled along the axes with a large second harmonic coefficient. Moreover, further problems arise such as inconvenient phase-matching temperature or Poynting-vector walk-off by the birefringence, limiting conventional SHG [35].

4.1.2 Quasi Phase Matching in Periodically Poled Lithium Tantalate

The limitations due to phase-matching can be overcome by spatial modulation of the second harmonic coefficient $d \equiv d(z)$. This technique is known as *quasi phase matching* (QPM) allowing for efficient SHG over the whole transparency region of a nonlinear crystal [35].

At low pump power and conversion efficiency, the second harmonic in the case of type-I SHG is given by [36]

$$E_s(L) \propto \int_0^L dz d(z) e^{-i\Delta k' z} \quad (4.7)$$

where L is the length of the crystal and the phase mismatch is defined as

$$\Delta k' = k_s - 2k_p = \frac{\pi}{\lambda_p/4(n_s - n_p)} \quad (4.8)$$

Substituting this result back in equation 4.7 reveals that the phase mismatch $\Delta k'$ leads to a change in sign after a distance $l_c = \frac{\lambda}{4(n_s - n_p)}$, called *coherence length* [36]. Hence, for a constant nonlinear coefficient d the amplitude of the signal field is zero after a propagation distance equal to an integer multiple of $2l_c$.

By inverting the sign of d every coherence length, the phase can be artificially matched and SHG is possible. A periodic inversion of d can be easily obtained growing a stack of thin wavers of the crystal, each rotated by 180° [36] because second-order nonlinear crystals cannot have an inversion symmetry [34].

The effect of QPM is illustrated in Figure 4.2. The sign of the second-order nonlinear coefficient d is periodically altered every coherence length l_c , leading a growth of SH intensity.

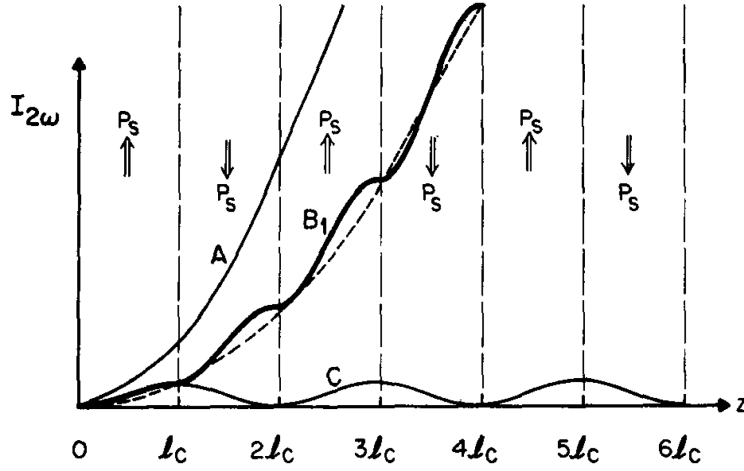


Figure 4.2: Second harmonic intensity for phase-matching (A), quasi-phase-matching (B_1) and phase mismatch (C). To achieve QPM the sign of the second-order nonlinear coefficient is altered every coherence length l_c . Image taken from [36].

The integral in equation 4.7 can be evaluated in the case of a periodic change of d , yielding [36]

$$|E_s|^2 \approx \left(\frac{\omega_p |E_p|^2}{n_s c} \right)^2 \left(\frac{2|d|L}{\pi} \right)^2 \text{sinc}^2 \left(\frac{\Delta k L}{2} \right) \quad (4.9)$$

where $\Delta k = \Delta k' - 2\pi/\Lambda$ and $\Lambda = 2l_c$.

For a Gaussian beam profile, $|E_0|^2 = I_0 = 2P/(\pi w_0^2)$, where P is the average power of the beam and w_0 the waist size. Therefore,

$$P_s \approx \frac{\omega_p^2 |d|^2 L^2}{\pi^3 w_0^2 n_s^2 c^2} P_p^2 \text{sinc}^2 \left(\frac{\Delta k L}{2} \right) \quad (4.10)$$

i.e. the SH power is proportional to the pump power squared, but attenuated by a factor $(2/\pi)^2$ compared to conventional phase-matching [35]. However, since QPM can be achieved along any crystal axis, the direction with the largest nonlinear coefficient can be chosen to be altered, yielding an effective increase of SH efficiency for most wavelengths compared to conventional SHG. Furthermore, by tuning the temperature of the crystal and hence its length, any wavelength that is transmitted can be brought to QPM, without changing the angle of incidence of the pump beam.

The above formula is only valid for low powers. For high pump power, the SHG efficiency $\eta_{SHG} = P_s/P_p$ can be calculated using coupled-wave theory [34]

$$\eta_{SHG} = \tanh^2 \left(2L \sqrt{\frac{d_{eff}^2 \eta^3 \omega_p^2 P_p}{\pi w_0^2}} \right) \quad (4.11)$$

where $\eta = \eta_0/n_p$ is the impedance of the medium. For QPM, the second-order nonlinear coefficient has to be scaled according to [36] by $d_{eff} = 2|d|/\pi$.

Periodically Poled Lithium Tantalate One crystal often used for QPM is periodically poled LiTaO₃ (PPLT) due to its very large second-order nonlinear coefficient⁶ of $d_{33} \approx 30 \text{ pm V}^{-1}$ [37]. In the following, a model for the temperature dependence of QPM in PPLT, which was used in this thesis, is derived.

The temperature dependence of the crystal length is described by the heuristic formula

$$L(T) \approx L(T_0) (1 + \alpha(T - T_0) + \beta(T - T_0)^2) \quad (4.12)$$

with $T_0 = 298 \text{ K}$, $\alpha = 16.2 \times 10^{-6} \text{ K}^{-1}$ and $\beta = 5.9 \times 10^{-9} \text{ K}^{-2}$ for PPLT [37].

The temperature of the crystal is tuned by an oven, but the absorption of light must also be considered. The temperature change due to absorption of the fundamental and second harmonic is [38]

$$\Delta T \approx \frac{(\alpha_p \cdot P_p + \alpha_s \cdot P_s)}{2\pi w_0 \kappa} \quad (4.13)$$

where the numerical values for both absorption coefficients $\alpha_s = 2 \times 10^{-5} \text{ m}^{-1}$ and $\alpha_p = 5 \times 10^{-5} \text{ m}^{-1}$ and the linear thermal expansion coefficient $\kappa = 5 \text{ W m}^{-1} \text{ K}^{-1}$ were taken from [37].

For the maximum intensity of the pump laser that was used in the experiment, the Kerr effect, i.e. the change of refractive index due to a high electric field strength, is negligible. Also the refractive index does not change significantly over the observed temperature range required for achieving QPM.

Figure 4.3 shows the theoretical phase-matching temperature as well as the relative SHG conversion efficiency. The measured temperatures diverge from the calculated values, most likely because the absorption of the stacked crystal is higher than in bulk

⁶The second order nonlinear coefficient of PPLT is very similar to PPLN (periodically poled LiNaO₃), another widely used crystal for QMP [37]. Therefore it is possible to compare the results found in this thesis using a PPLT crystal with what was reported in [11] for PPLN

LiTaO₃. Furthermore, the efficiency at a pump power of $P_p \approx 34.7$ W is lower than theoretically expected, indicating that the approximation of low power and conversion efficiency is no longer valid.

Indeed, Figure 4.8 indicates, that the approximation of low power only holds up to a pump power of ~ 20 W, up to which the SH power increases quadratically with P_p .

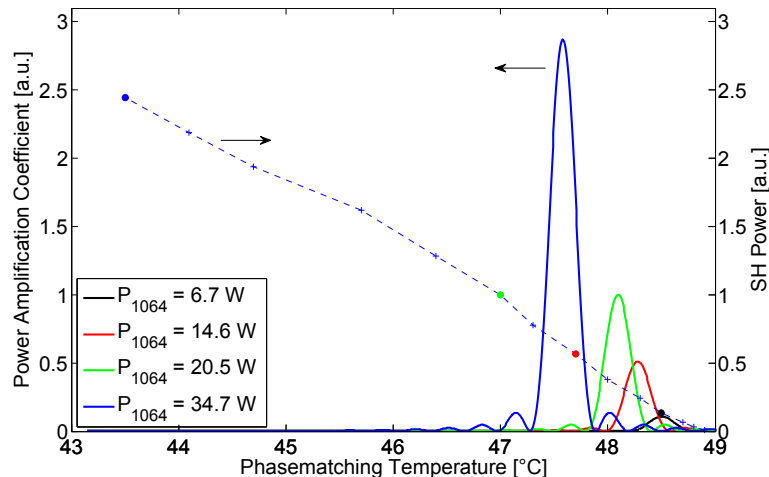


Figure 4.3: Theoretical phase-matching temperature dependence of the SHG efficiency (solid lines) normalized to the efficiency at 20 W and the experimentally measured values. The dots mark the measured values corresponding to the theoretically calculated efficiencies. Note that the temperature for the measured values is the temperature of the oven containing the PPLT crystal and not the actual temperature inside the crystal. For the theoretical curve the number of domains in the PPLT crystal was chosen such that the phase-matching temperature at 6.7 W corresponded to the measured temperature.

4.1.3 Experimental Setup and Results

The laser used to generate the fundamental harmonic is a diode-pumped Nd:YAG laser with four cascaded amplifying stages (Coherent Inc. Mephisto MOPA [39]) producing 56 W of output power at 1064 nm with a specified linewidth fluctuation of 1 kHz s^{-1} .

As shown in Figure 4.4, the amplifier operates properly only at the maximum pump current of $I_{\text{max}} = 49.50$ A as specified in the data sheet. Hence, the output power was always set to its maximum value $P_{\text{max}} = 56.35$ W. For controlling the amount of power in the setup and thus the power of the second harmonic light, a half-wave plate and a subsequent Glan-Laser⁷ polarizer were used. The wave plate was calibrated once and allowed for reproducible control of the power between ~ 10 mW and 43.1 ± 0.3 W. This calibration is shown in Figure 4.5.

⁷A Glan-Taylor polarizer suitable for high-power applications.

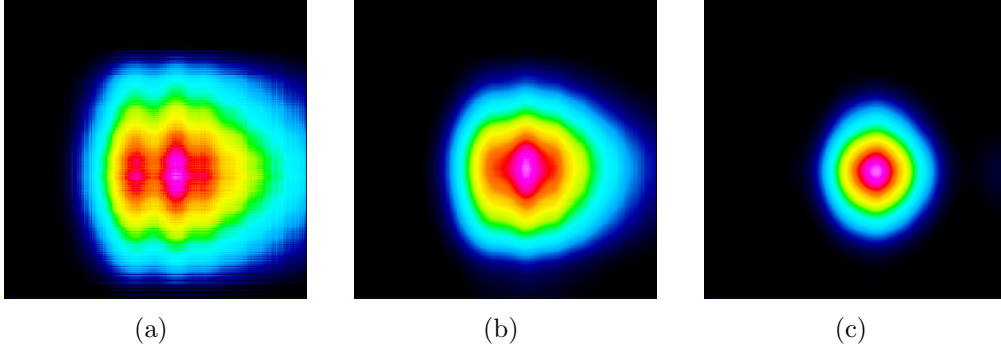


Figure 4.4: Beam profile of the fundamental harmonic at various pump currents corresponding to 11, 30 and 56 W. The beam profile is Gaussian and as specified in the data sheet only at the maximum pump current of $I_{\max} = 49.50$ A (corresponding to 56 W output power).

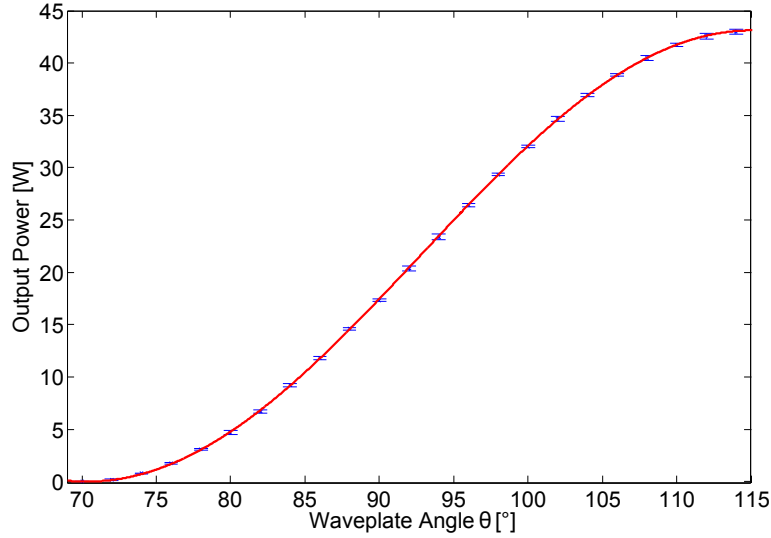


Figure 4.5: Amount of power transmitted by the Glan-Laser polarizer as a function of rotation angle θ of the half-wave plate. The measured data corresponds well with the calculated formula $I(\theta) \propto 4 \sin^2 \theta \cos^2 \theta$ (fitted curve, see A.2 for derivation).

The beam was then focused into a 20 mm long PPLT crystal (HC Photonics PP-MgO:SLT⁸ [40]) which allowed for quasi-phasematched second harmonic generation. The focusing parameter $\xi = l/b$ was fine-tuned by changing the distance between the lenses of telescope T_1 . Here l denotes the length of the crystal and $b = 2z_0$ is the confocal parameter of the focused Gaussian beam. For temperature control and stabilization, the crystal was mounted in an oven and connected to a closed-loop PID temperature controller.

Figure 4.6 summarizes the SHG efficiencies for various focusing parameters ξ at low powers. The best efficiency was achieved with a focusing of $\xi = 1.3$. This result diverges from the optimal focusing of $\xi_{\text{opt}} = 1.84$ derived for phase-matched SHG [41]. However, the spot size of $w_0 = 35.0 \pm 2 \mu\text{m}$ inside the crystal is very close to what the data sheet suggests and what was also reported for a 30 mm crystal in [11].

⁸The abbreviation stands for *periodically poled magnesium oxide doped stoichiometric lithium tantalate*.

The discrepancy can be explained by the complex structure of the crystal and similar discrepancies were found elsewhere (see e.g. for PPLN [42]).

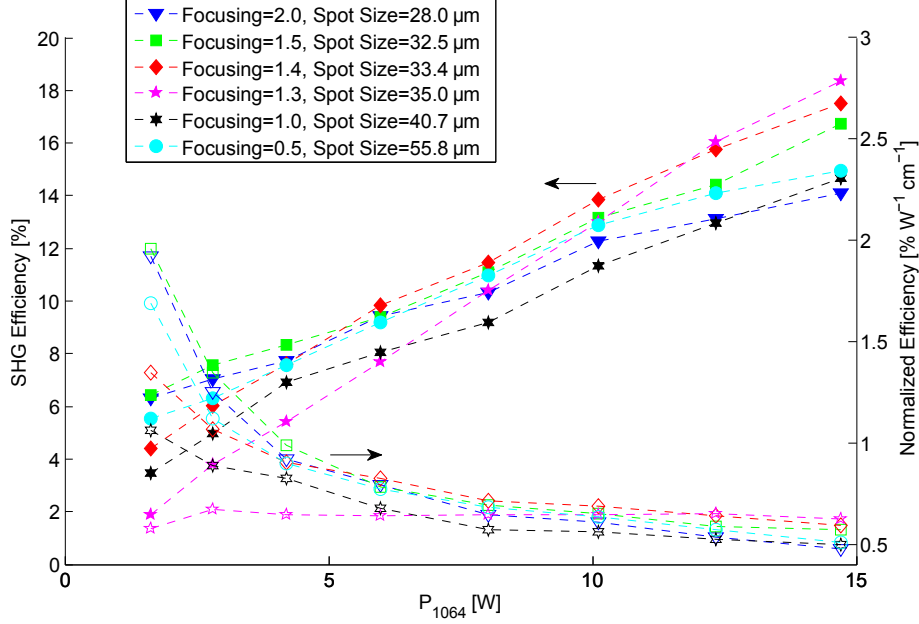


Figure 4.6: SHG efficiency for different focusing parameters $\xi = l/b$. The high efficiencies at low power are explained by the experimental setup. At low pump power the intensity is not high enough for SHG and therefore more light of the fundamental harmonic is transmitted. By using two dichroic mirrors in series (for the measurement of the $\xi = 1.3$ curve) this effect was suppressed. The transmittance of the second beam splitter was 95% and for comparison the result was scaled accordingly.

Figure 4.7 shows a measurement of the SH efficiency for high pump powers. The maximum efficiency achieved was $25.5 \pm 0.5\%$ at a pump power of $P_{1064} = 34.6 \pm 0.2 \text{ W}$ ($\eta_{\text{norm}} = 0.45 \pm 0.05\% \text{ W}^{-1} \text{ cm}^{-1}$). The normalized efficiency at a pump power of $P_{1064} = 29.3 \pm 0.1 \text{ W}$ was $\eta_{\text{norm}} = 0.41 \pm 0.05\% \text{ W}^{-1} \text{ cm}^{-1}$ which is slightly larger than $\eta = 0.37\% \text{ W}^{-1} \text{ cm}^{-1}$, reported in [11].

For high pump powers the efficiency is below the theoretically expected value which was fitted to the data. This indicates that higher-order nonlinear effects such as non-uniform heating and thus local deformation of the crystal become noticeable.

From the least-squares fit the nonlinear second order coefficient was extracted. Its value of $d = 3.10 \pm 0.04 \text{ pm V}^{-1}$ is much smaller than the value of $d_{33} = 13.8 \text{ pm V}^{-1}$ at $\lambda = 1064 \text{ nm}$ for bulk LiTaO_3 found in literature [37]. The discrepancy can most likely be explained by the periodical polling of the crystal. Perfect phase matching is only obtained when the domains have all exactly the same length. Small changes due to for example imperfect crystal growth or temperature gradients therefore prevent perfect phase matching from occurring, limiting the conversion efficiency.

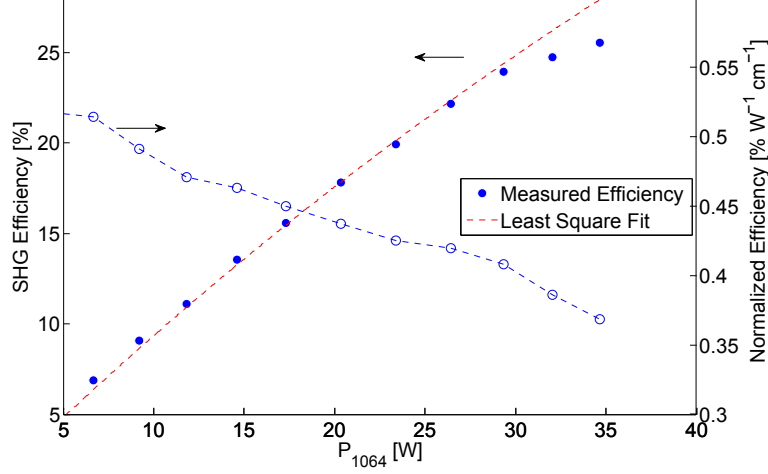


Figure 4.7: Measurement of SH efficiency for high pump power with a focusing of $\xi = 1.3$. Beyond $P_p > 35$ W the second harmonic did not stabilize and it was not possible to take data. The theoretical curve for the efficiency is fitted to the values (the two last data points were discharged for the fit), indicating a drop-off for powers beyond ~ 30 W.

It was not possible to increase the pump power beyond ~ 35 W because it was not possible to control the temperature of the PPLT crystal well enough to stabilize the SH power. Equation 4.10 implies that the change of power with respect to temperature fluctuations increases as $\frac{dP_s}{dT} \propto P_s^2$. Since the oven controller was stabilizing the temperature to $T_{set} \pm 0.1^\circ\text{C}$, for high enough pump powers the oscillation of the temperature about the set-point led to a notable change in SH power.

For 20 W of pump power, the change of SH power was calculated to be $\frac{dP_s}{dT} \times \Delta T \approx 0.06$ W for a temperature drift of $\Delta T = 0.1^\circ\text{C}$ using equation 4.10. The order of magnitude of this estimate is in good agreement with what was observed experimentally.

These calculations did not include the change in crystal heating due to changing second harmonic power, leading to complex nonlinear dynamics at higher powers. The measurement of SH power was stopped when the fluctuations were as large as ~ 0.5 W, thus limiting the maximum SH power to 8.4 ± 0.3 W.

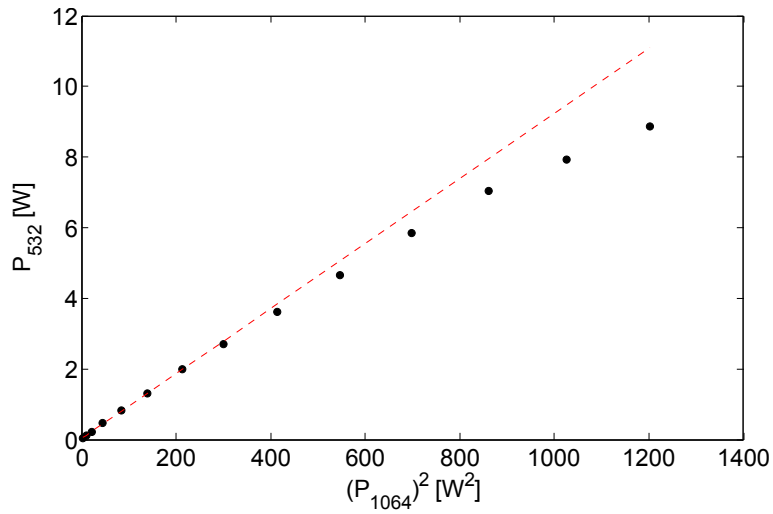


Figure 4.8: The SH power increased quadratically up to a fundamental power of ~ 20 W in good agreement with the results reported in [11].

After splitting the fundamental from the second harmonic using a dichroic beam splitter, the frequency-doubled light was coupled into a *photonic crystal fibre* (PCF). The PCF was used for cleaning the beam profile, i.e. removing the ellipticity and making sure that only a $\text{TEM}_{0,0}$ spatial mode was present. Furthermore, any residual light of the fundamental beam was rejected by the fibre. The ellipticity of the fibre mode was measured to be 1.00 and is shown in the inset of Figure 4.9.

Due to the high power of the laser, a polarization maintaining large core PCF (NKT Photonics LMA-PM-15) was used which was able to handle the power and suffered much less from Brillouin scattering than standard single-mode fibres do [43].

It is important to note, that the polarization of the incoming beam must match the polarization mode of the fibre. When the polarization is not well aligned or the fibre is not even polarization maintaining, the two (linear) polarization modes of the fibre can randomly interfere due to impurities or strain in the glass [34] which then lead to unwanted (random) fluctuations of the output power.

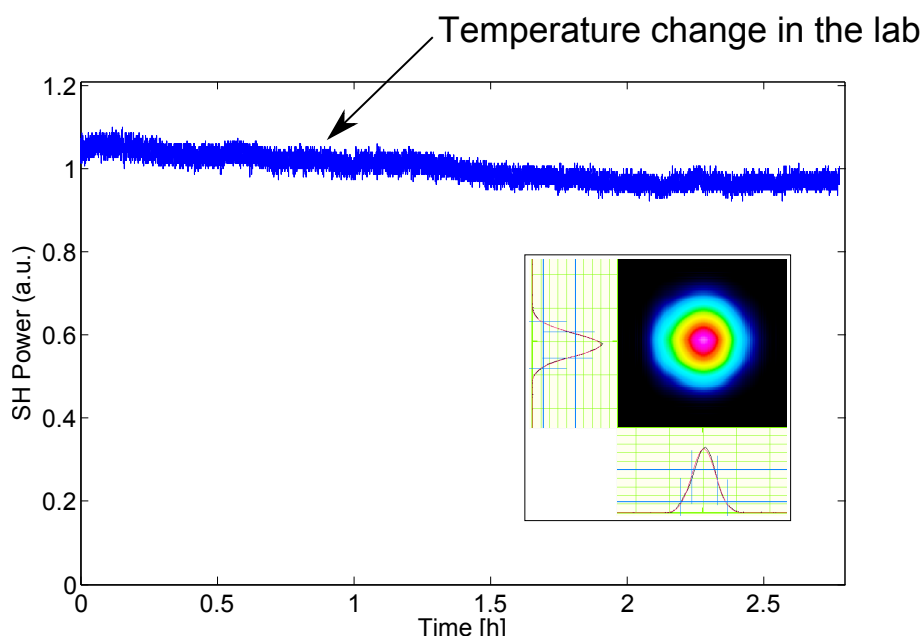


Figure 4.9: Fluctuation of the SH power at ~ 500 mW over 2.7 h normalized to the mean value. Due to a change in temperature in the lab, the power drifted slowly, but stabilized again after ~ 1.5 h. The power fluctuated by $\sim 1.2\%$ when neglecting the overall drift. The inset shows the beam profile cleaned by the PCF. The ellipticity of the beam was measured to be 0.88 before and 1.00 after the fibre. The SH beam is elliptical because the output beam of the Nd:YAG has also an ellipticity of 0.89.

4.2 High Finesse Cavity

As shown in Section 3.1 the Gaussian mode of a cavity can be used for creating a fully confining dipole potential in three dimensions. In order to test whether the frequency doubled laser presented above can be used for trapping, a *high finesse* (hf) cavity, designed by M. Marinelli in his master thesis [10], was characterized.

For stabilizing the laser frequency to the resonance of the cavity a *Pound-Drever-Hall* (PDH) locking scheme [44] was implemented, briefly discussed in the following. Afterwards, the experimental results are presented.

4.2.1 Cavity Frequency Stabilization (Pound-Drever-Hall Locking)

The frequency stability of lasers is a major concern in various fields. In the case of optical trapping for example, a drifting laser frequency changes the wavevector \mathbf{k} as well as the detuning Δ_{ij} , leading to a fluctuation of the potential minima and trap depth. Even more important, the linewidth of the cavity is only $\Delta\nu = 308 \text{ kHz}$ [10] and for larger fluctuations no light will be coupled in.

One commonly used technique is the PDH scheme which allows for very precise measurement of the frequency of a cavity using heterodyne detection [44]. Here only the main ideas of PDH locking are discussed; a rigorous treatment can be found for example in [45].

The reflection from a cavity is the coherent sum of the light directly reflected and the leakage beam [45]. The resonance condition implies that the light inside the cavity must accumulate a phase shift of $\phi = 2\pi n$ over each round-trip where n is an integer number [34]. On the other hand, the light directly reflected from the cavity mirror only accumulated a phase shift of π . Therefore, on resonance, the reflected beam and the light leaking out of the cavity destructively interfere. By modulating the phase of the incoming light with an *electro-optic modulator* (EOM), the interference signal can be detected in a lock-in type measurement.

When the laser frequency is detuned from the resonance of the cavity, the intensity of the interference pattern changes as depicted in Figure 4.10. This signal can be used to discriminate by how much cavity and laser are detuned and a *proportional-integral* (PI) control-loop can be used to correct the detuning.

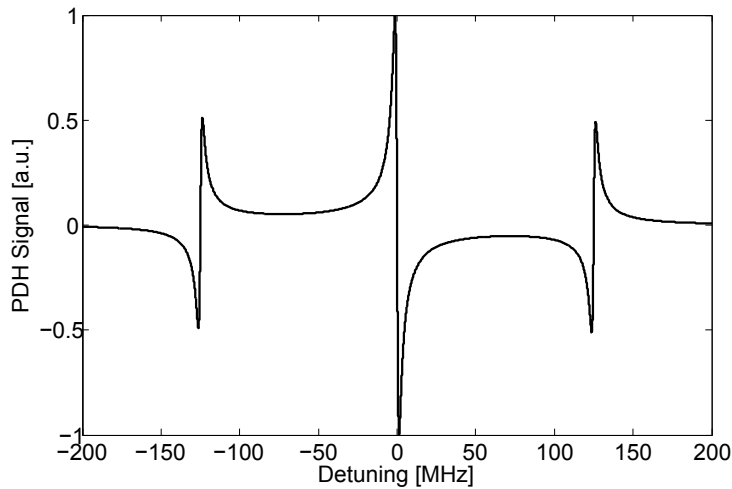


Figure 4.10: PDH signal for a modulation frequency $\Omega = 125 \text{ MHz}$ and a finesse of $\mathcal{F} = 10^4$.

For locking the laser to the cavity two possibilities exist. Either the frequency of the laser is changed to match the cavity mode or alternatively the length of the cavity is locked to the laser. However, both methods have their disadvantages.

One of the cavity mirrors was mounted on a piezo shear plate which allowed for sweeping the cavity length over more than one *free spectral range* (FSR). The downside of controlling the length of the cavity was that the inertia of the mirror mount severely limited the bandwidth of the controller.

On the other hand, it was possible to directly modulate the laser frequency by up to 100 kHz⁹. However, the tuning range was limited to around ± 25 MHz, which is much less than the designed FSR of 3.1 GHz of the cavity, rendering correction of larger long-time drifts impossible.

In the setup the digital EVIL¹⁰-controller, developed by L.E. De Clercq and V. Negnevitsky in our group, was modified such that the *proportional* (P) and *integrator* (I) values were output on two different channels. Therefore it was possible to exploit the advantages of both locking methods. Fast drifts were corrected by the P output, directed to the piezo modulator of the laser, while the I value was used to correct for slow long-term drifts by adjusting the length of the cavity.

4.2.2 Experimental Setup

The hf cavity consisted of two highly reflecting mirrors ($R = 0.9998$) in a near concentric configuration with a finesse of $F \approx 10000$, a linewidth of $\Delta\nu = 308$ kHz and a FSR of 3.1 GHz. The power building up in the cavity was estimated to be $P_{in} = 950$ W for an injection power of 600 mW [10].

The final goal of this project is to perform adiabatic transport of a trapped ion from a rf to a dipole trap as presented in [6]. Out of the two ion species available to date in our lab (^{40}Ca and ^9Be), calcium is better suited for optical trapping but no Doppler cooling and qubit operation are possible [10]. Thus, only a proof of principle is possible in the current system where the ion is first cooled in the rf trap and then adiabatically transported to the optical lattice.

The best suited trap in our lab for such experiments is the two dimensional surface trap based on PCF technology [46], in the following called the *fibre trap*. Figure 4.11 shows a model of how the cavity is integrated into the trap structure. The ring holder on which the two cavity mirrors are mounted fits exactly into the vacuum chamber around the tip of the PCF which forms the fibre trap.

The hollow structure of the PCF is filled with gold wires, serving as electrodes to generate a confining pseudopotential 88 μm above the surface [46]. The tip of the fibre is therefore placed slightly below the centre of the cavity, close to the waist of the mode. The ion can then be loaded and cooled in the fibre trap with the optical lattice turned off. In a second step the rf drive field is ramped down while the power of the light coupled into the cavity is gradually increased, providing an adiabatic transition between the two trapping potentials. For readout and re-cooling the ion is then transferred back to the fibre trap.

4.2.3 Results

For testing the cavity outside the vacuum chamber of the fibre trap, first a small box was used to protect the cavity from dust. In a second step the cavity was then moved

⁹According to the data sheet.

¹⁰Electronically Variable Interactive Lockbox

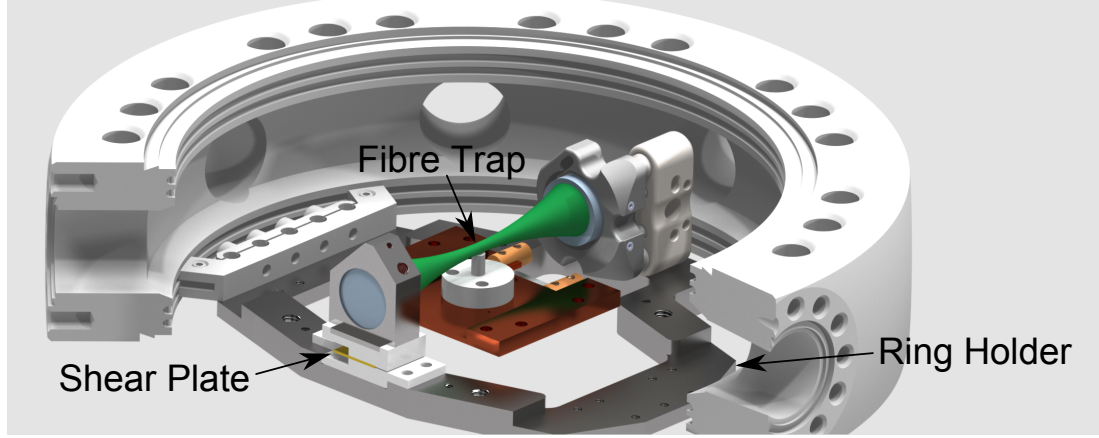
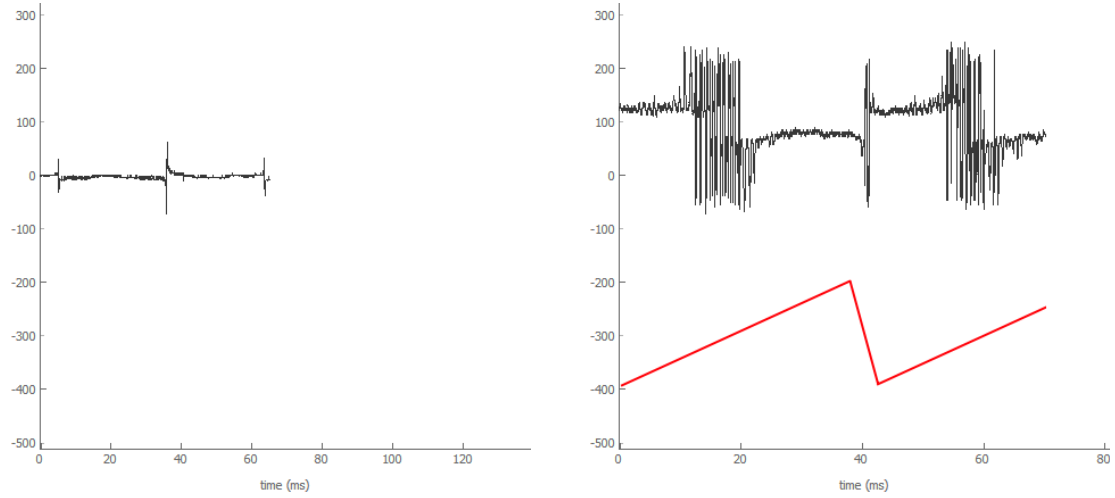


Figure 4.11: CAD model of the hf cavity by M. Marinelli. The cavity is mounted on a ring holder which fits into the vacuum chamber of the fibre trap such that the waist of the cavity mode coincides with the centre of the rf trapping potential.

into a vacuum chamber, dedicated to testing the cavity.

Figure 4.12 shows the measured PDH signal when scanning the cavity length. When detuning the cavity more than ± 125 MHz, which was the modulation frequency of the EOM, the characteristic sidebands of the PDH signal are visible (Figure 4.12a) and the sharpness of the peaks indicates the high finesse of the cavity.



(a) Measured PDH signal when scanning the cavity mirror.

(b) PDH signal for smaller scanning range around the resonance peak. Instead of one, several peaks are visible. The red curve illustrates the ramp of the frequency of the laser.

Figure 4.12: PDH signal of the cavity.

When the cavity length or equivalently the laser frequency is detuned by only a small amount from resonance (Figure 4.12b), several peaks appear in the PDH signal over one ramp. This indicates fluctuations faster than the scanning frequency. Since it was not possible to resolve these peaks individually, i.e. scanning the frequency of the laser faster than the fluctuations, it was also not possible to lock the cavity.

This is shown in Figure 4.13. When the control-loop was turned on, the transmission of the cavity was only high for at most ~ 11 ms before a disturbance occurred which unlocked the cavity for a short time. By using a cardboard box for acoustic isolation, it was possible to extend the timespan over which the cavity was locked to ~ 31 ms, which indicated that acoustic noise prevented the cavity from being locked.

Furthermore, 4.13c shows that it is very important to decouple the cavity from the optical table. When the cavity was directly connected to the table, the transmission signal clearly showed a repetitive drop with a frequency of 1.4 Hz. This is the characteristic frequency of the pulse tube of the cryorefrigerator used for the surface ion trap experiment set up on the same optical table [47].

By decoupling the cavity from the table using three damping rubber pads, the signal vanished and it was possible to lock the cavity for several milliseconds as discussed above.

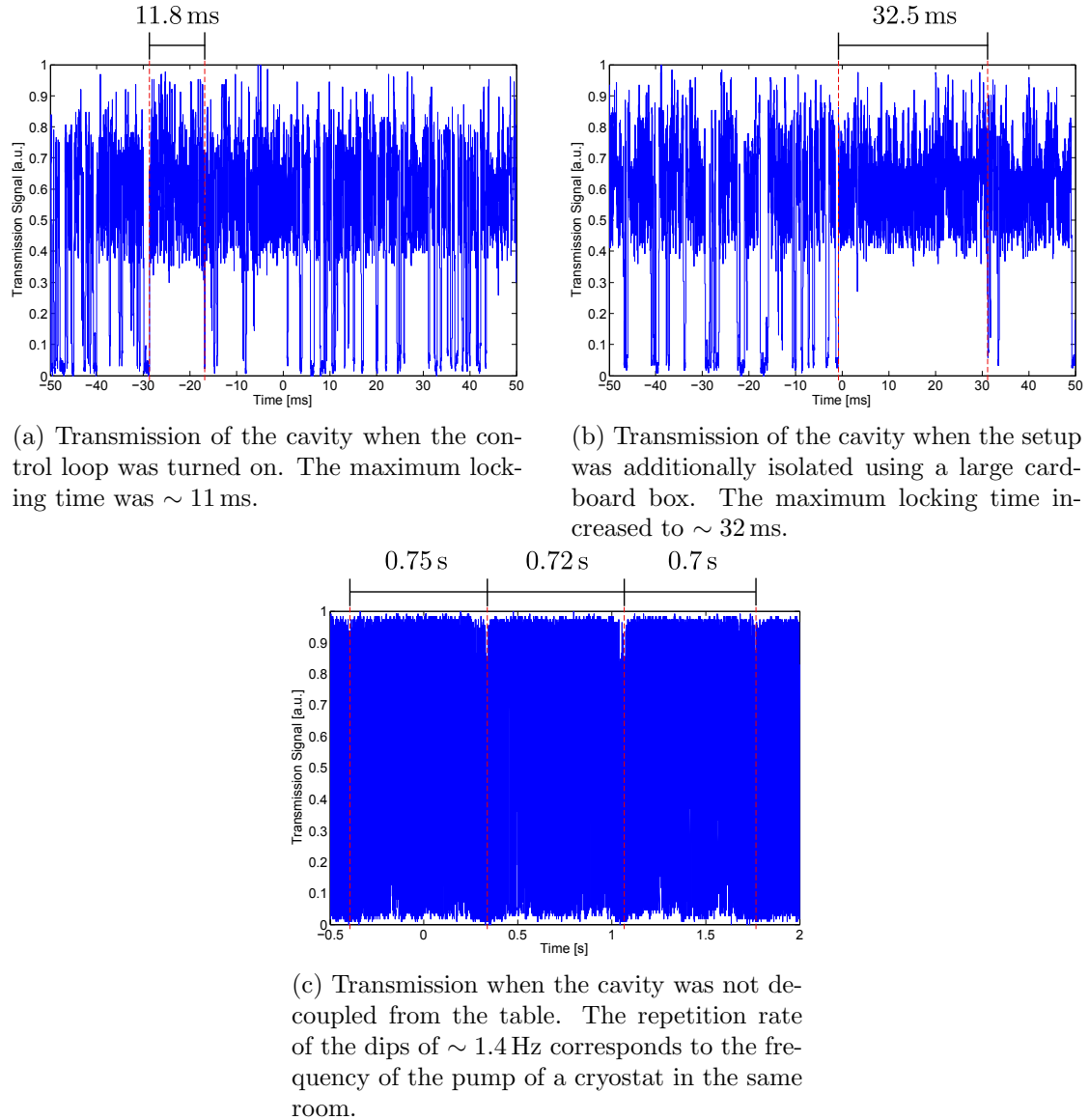


Figure 4.13: Transmission signal of the hf cavity when the control-loop was turned on.

Since it was not possible to lock the cavity and the test with the cardboard box indicated that the problem was at least partially caused by acoustic disturbances, the

cavity was placed in a vacuum chamber. The chamber was also much more rigid and thus it was expected that problems related to vibrations of the box initially containing the cavity could be resolved.

Indeed, as shown in Figure 4.14, the time over which it was possible to lock the cavity increased dramatically. Locking times of up to ~ 4 s were observed. However, the transmission signal still showed a periodic modulation. By analysing the spectrum components at 1.4 Hz and 4.2 Hz, associated to the pump of the cryorefrigerator mentioned before, were found.

Observing the interference pattern between light reflected from the cavity and light reflected off several optical components in the beam path led to the conclusion that the beam pointing varied periodically with a frequency of ~ 1.4 Hz. This on the other hand also implies that the incoupling efficiency to the cavity is oscillating at the same frequency.

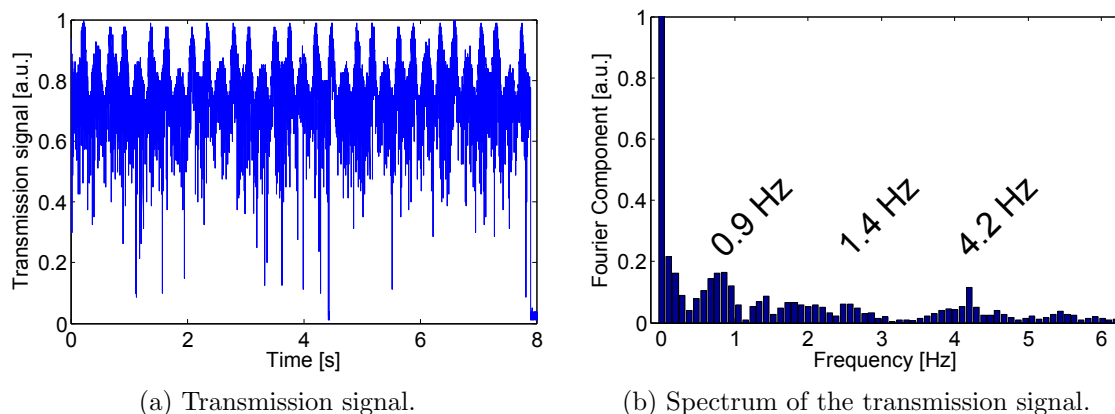


Figure 4.14: Transmission of the hf cavity in vacuum.

Before further test of the hf cavity can be performed, the beam pointing must be stabilized either passively by decoupling the optical tables or by active control of the beam pointing using piezoelectric adjustable mirrors connected up to a control system. The apparently simplest approach of separating the table on which the cryostat stands from the rest of the optical setup is, however, at the moment not possible and hence further work on the cavity has to be postponed until the problem is solved.

5 Summary and Outlook

It was shown in this thesis that it is in principle possible to lock a narrow linewidth frequency-doubled laser to the build up cavity designed for optical dipole trapping of ions. However, it was not possible to fully investigate the properties of the cavity, i.e. finesse, photon lifetime, etc. because vibrations caused by the pulse tube used for cooling of the surface trap experiment on the same optical table prevented stable locking. Currently, it is not possible to decouple the two experiments and therefore some kind of active beam stabilization might be required before further experiment can be performed.

It was also shown that the optimal beam focusing for phase-matched SHG [41] cannot be applied to quasi phase-matched periodically poled crystals as also reported for example in [42], contradicting the claim in [11].

The benchmark of BEM and FEM suggested that the commercial software can be used as well and, in some situations, even performs better. This can especially be noticed for curved surfaces and in close proximity to the electrodes. Since a MATLAB[®]-script was written, that converted the results of the FEM simulation to the same data format as output by BEM, the analysis tools that were used so far still work, making BEM and FEM interchangeable.

Finally, a novel type of ion trap was presented, that allows for trapping in an optical lattice, supported by static electric fields. This trap has the further advantage that it provides large apertures for controlling and detection of the ions.

A simulation algorithm was then outlined which allows for solving the classical many-body equation of motion of charged particles in such a trap configuration. This algorithm was then used to simulate the electro-optical hybrid trap. It was shown, that an adiabatic transfer between a conventional rf ion trap to the optical lattice has to be performed in order to get stable confinement. Such a simulation is also very close to experimental realization, for example reported in [6]. The stability of the trap was investigated for various ramp times $\Delta\tau$ and dc voltages, which, in the confining cases, always led to a spherical arrangement of the ions. It was shown that the final separation of the ions depended on both the applied voltage as well as the number of ions loaded to the trap.

References

- [1] M.A. Nielsen and I.L. Chuang, *Quantum Computation and Quantum Information*. 10th edition (Cambridge University Press, Cambridge 2010).
- [2] R.P. Feynman, *Simulating Physics with Computers*, Int. J. Theoret. Phys. **21** (6-7), 467-488 (1982).
- [3] J.I. Cirac and P. Zoller, *Goals and opportunities in quantum simulation*, Nat.Phys. **8** (4), 264-266 (2012).
- [4] R. Blatt and C.F. Roos, *Quantum simulations with trapped ions*, Nat.Phys. **8** (4), 277-284 (2012).
- [5] M. Johanning, A.F. Varón and C. Wunderlich, *Quantum simulations with cold trapped ions*, J. Phys. B **42**, 154009 (2009).
- [6] C. Schneider et al., *Optical trapping of an ion*, Nature Photon. **4**, 772-775 (2010).
- [7] M. Enderlein et al., *Single ions trapped in a one-dimensional optical lattice*, Phys. Rev. Lett. **109** 233004 (2012).
- [8] T. Huber et al., *A far-off-resonance optical trap for a Ba^+ ion*, Nat. Commun. **5**, 5587 (2014).
- [9] R. Grimm, M. Weidemüller and Y. B. Ovchinnikov, *Optical dipole traps for neutral atoms*, Adv. At., Mol., Opt. Phys. **42**, 95-170 (2000).
- [10] M. Marinelli, *High finesse cavity for optical trapping of ions*, Master Thesis, ETH Zurich (2014).
- [11] G.K. Samanta et al., *Stable, 9.6 W, continuous-wave, single-frequency, fiber-based green source at 532 nm*, Opt. Lett. **34**, 10, 1561-1563 (2009).
- [12] D. Leibfried et al., *Quantum dynamics of single trapped ions*, Rev. Mod. Phys. **75**, 281-324 (2003).
- [13] R.B. Blakestad, *Transport of trapped-ion qubits within a scalable quantum processor*, Ph.D. Thesis, University of Colorado (2010).
- [14] W. Paul, *Electromagnetic traps for charged and neutral particles*, Rev. Mod. Phys. **62**, 531-540 (1990).
- [15] D.J. Wineland et al., *Experimental issues in coherent quantum-state manipulation of trapped atomic ions*, J. Res. Natl. Inst. Stand. Technol. **103** (3), 259-328 (1998).
- [16] M. Cetina, A.T. Grier and V. Vuletić, *Micromotion-induced limit to atom-ion sympathetic cooling in paul traps*, Phys. Rev. Lett. **109**, 253201 (2012).
- [17] D.W. Pepper and J.C. Heinrich, *The Finite Element Method*. 2nd edition (Taylor & Francis, New York, 2006).
- [18] J.D. Jackson, *Classical Electrodynamics*. 3rd edition (John Wiley & Sons, Hoboken, 1999).
- [19] K. Signer et al., *Colloquium: Experiments with atomic quantum bits - essential numerical tools*, Rev. Mod. Phys. **82**, 2609-2632 (2009).

- [20] D. Cubric et al., *Comparison of FDM, FEM and BEM for electrostatic charged particle optics*, Nucl. Instr. Meth. Phys. Res. A **427**, 357-362 (1999).
- [21] Y.J. Liu and N. Nishimura, *The fast multipole boundary element method for potential problems: A tutorial*, Eng. Anal. Bound. Elem. **30**, 371-381 (2006).
- [22] COMSOL Inc. [Online], 11.04.2015, <https://www.comsol.com>.
- [23] C. Zipkes et al., *A trapped single ion inside a Bose–Einstein condensate*, Nature **464** (18), 388-391 (2010).
- [24] T. Pruttivarasin et al., *Trapped ions in optical lattices for probing oscillator chain models*, New J. Phys. **13**, 075012 (2011).
- [25] C.A. Schrama et al., *Novel miniature ion traps*, Opt. Commun. **101**, 32-36 (1993).
- [26] J.R.C. Pita, *Design, development and operation of novel ion trap geometries*, Ph.D. Thesis, Imperial College London (2007).
- [27] A. W. Sandvik, *Numerical solutions of classical equations of motion* [Online], 22.02.2015, <http://physics.bu.edu/py502/lectures3/cmotion.pdf>.
- [28] N. Grønbech-Jensen and O. Farago, *A simple and effective Verlet-type algorithm for simulating Langevin dynamics*, Mol. Phys. **111** (8), 983-991 (2013).
- [29] E. Hairer, C. Lubich and G. Wanner, *Geometric numerical integration illustrated by the Störmer–Verlet method*, Acta Numer. **12**, 399-450 (2003).
- [30] F.G. Major, V.N. Gheorghe and G. Werth, *Charged Particle Traps* (Springer, Berlin, 2005).
- [31] C.J. Foot, *Atomic Physics* (Oxford University Press, Oxford, 2005).
- [32] P. Staunum, *Quantum Optics with trapped calcium ions*, Ph.D. Thesis, University of Aarhus (2004).
- [33] C. Ospelkaus et al., *Microwave quantum logic gates for trapped ions*, Nature **476**, 181-184 (2011).
- [34] B.E.A. Saleh and M.C. Teich, *Fundamentals of Photonics*. 2nd edition (John Wiley & Sons, Hoboken, 2007).
- [35] L.E. Myers et al., *Quasi-phase-matched optical parametric oscillators in bulk periodically poled LiNbO₃*, J. Opt. Soc. Am. B **12** (11), 2102-2116 (1995).
- [36] M.M. Frejer et al., *Quasi-Phase-Matched Second Harmonic Generation: Tuning and Tolerances*, IEEE J. Quant. Electron. **28** (11), 2631-2654 (1992).
- [37] D.N. Nikogosyan, *Nonlinear Optical Crystals: A Complete Survey* (Springer, Berlin, 2005).
- [38] R.M. Wood, *Laser induced damage thresholds and laser safety levels. Do the units of measurement matter?*, Opt. Laser Technol. **29** (8), 517-522 (1997).
- [39] Coherent Inc. Mephisto MOPA laser system [Online], 21.03.2015, <http://www.coherent.com/products/index.cfm?2067/Mephisto-MOPA>.

- [40] HC Photonics Corp. [Online], 21.03.2015, <http://www.hcphotonics.com>.
- [41] G.D. Boyd and D.A. Kleinman, *Parametric Interaction of Focused Gaussian Light Beams*, J. Appl. Phys **39**, 8, 3597-3639 (1968).
- [42] A.C. Wilson et al., *A 750-mW, continuous-wave, solid-state laser source at 313 nm for cooling and manipulating trapped $^9\text{Be}^+$ ions*, Appl. Phys. B **105**, 741-748 (2011).
- [43] A. Kobayakov, M. Saurer and D. Chowdhury, *Stimulated Brillouin scattering in optical fibers*, Adv. Opt. Photonics **2** (1), 1-59 (2010).
- [44] R.W.P. Drever et al., *Laser phase and frequency stabilization using an optical resonator*, Appl. Phys. B **31**, 97-105 (1983).
- [45] E.D. Black, *An introduction to Pound–Drever–Hall laser frequency stabilization*, Am. J. Phys. **69**, 1, 79-87 (2001).
- [46] F. Lindenefelser et al., *An ion trap built with photonic crystal fibre technology*, Rev. Sci. Instrum. **86**, 033107 (2015).
- [47] M. Fadel, *Cryogenic setup for fast manipulation of the quantum motional states of trapped ions*, Master Thesis, ETH Zurich (2013).
- [48] K. Fisher, *Coherent control laser system for the quantum state manipulation of trapped ions*, Maser Thesis, ETH Zurich (2013).

A Appendix

A.1 List of Lenses

| | | |
|------------------------------------|------------------------|------------------------|
| Telescope T_1 | $f_1 = -30 \text{ mm}$ | $f_2 = 150 \text{ mm}$ |
| Telescope T_2 | $f_1 = 150 \text{ mm}$ | $f_2 = -75 \text{ mm}$ |
| Telescope T_3 | $f_1 = -30 \text{ mm}$ | $f_2 = 175 \text{ mm}$ |
| Focusing lens f_1 | $f = 300 \text{ mm}$ | |
| Focusing lens f_2 | $f = 250 \text{ mm}$ | |
| Collimating lens f_c | $f = 100 \text{ mm}$ | |
| Fibre incoupling lens f_a | $f = 18.15 \text{ mm}$ | |
| Fibre outcoupler f_o | $f = 15 \text{ mm}$ | |

A.2 Transmission of a Polarizing Beamsplitter

The transmission of linearly polarized light through a polarizing beamsplitter can be controlled by changing the angle of the polarization with respect to the ordinary and extra-ordinary axes of the birefringent crystal. A relation between angle of the polarization and transmitted power can be easily obtained from the matrix representation of polarization devices in the Jones formalism (described e.g. in [34]).

Consider a beam polarized along the $\hat{\mathbf{x}}$ axis. Its polarization can be represented by the unit vector $(1, 0)^T$. The Jones matrix of a half-wave plate rotated by an arbitrary angle θ with respect the $\hat{\mathbf{x}}$ axis can be found by applying the transformation

$$\begin{aligned} J_{\text{HWP}}(\theta) &= \begin{pmatrix} \cos \theta & \sin \theta \\ -\sin \theta & \cos \theta \end{pmatrix}^T \begin{pmatrix} 1 & 0 \\ 0 & -1 \end{pmatrix} \begin{pmatrix} \cos \theta & \sin \theta \\ -\sin \theta & \cos \theta \end{pmatrix} \\ &= \begin{pmatrix} \cos^2 \theta - \sin^2 \theta & 2 \sin \theta \cos \theta \\ 2 \sin \theta \cos \theta & \sin^2 \theta - \cos^2 \theta \end{pmatrix} \end{aligned} \quad (\text{A.1})$$

to the Jones matrix of a half-wave plate with the fast axis along $\hat{\mathbf{x}}$.

For simplicity, it can now be assumed, that only light polarized along $\hat{\mathbf{x}}$ is transmitted, hence its Jones matrix is simply given by

$$J_{\text{PBS}} = \begin{pmatrix} 1 & 0 \\ 0 & 0 \end{pmatrix} \quad (\text{A.2})$$

The intensity of a transverse electromagnetic wave is given by [34]

$$I = \frac{|\mathbf{E}_0|^2}{2\eta_0} \quad (\text{A.3})$$

where the impedance $\eta_0 \approx 377 \Omega$ in free space. Since the entries of the Jones vector describe the complex envelope of the electric field, the intensity is proportional to

$$\begin{aligned} I(\theta) &\propto |J_{\text{out}}(\theta)|^2 = |J_{\text{PBS}} J_{\text{HWP}}(\theta) J_{\text{in}}|^2 \\ &= \left| \begin{pmatrix} 1 & 0 \\ 0 & 0 \end{pmatrix} \begin{pmatrix} \cos^2 \theta - \sin^2 \theta & 2 \sin \theta \cos \theta \\ 2 \sin \theta \cos \theta & \sin^2 \theta - \cos^2 \theta \end{pmatrix} \begin{pmatrix} 1 \\ 0 \end{pmatrix} \right|^2 \\ &= 4 \sin^2 \theta \cos^2 \theta. \end{aligned} \quad (\text{A.4})$$

A.3 Interlock System

The interlock system that was developed during this thesis is based the initial design by K. Fisher [48] and utilizes a PCB board developed by Dr. B. Keitch in our group. The board was designed for general purpose logic operations and provides a *complex programmable logic device* (CPLD), several digital in and outputs as well as two relays. Furthermore, an Arduino Uno¹¹ can be easily connected, providing for example analogue readout of sensors.

The purpose of the interlock system was to monitor both temperature of a device and, at the same time, the flow of cooling water for example of a laser. In case of over-temperature the interlock system was designed to trip the internal interlock circuit of the monitored device by opening one of the relays. Furthermore, in case of a reduced water flow, e.g. due to a leakage in the cooling system, the interlock was able to close the main valve of the cooling circuit as well as shutting down the device.

The schematics of the interlock circuit is depicted in Figure A.1. The Arduino is used for analogue readout of the temperature and flux sensors and deciding whether the interlock has to be tripped. If this is the case, the Arduino sends a digital signal to the CPLD chip which then opens the correct relay.

For maximum reliability, the CPLD and the Arduino monitored each other by constantly sending pulse sequence between each other. If for example the Arduino is not responding any more, the CPLD immediately trips both interlock circuits to prevent any possible damage.

When the interlock was tripped, the circuit can only be reset by pressing a reset button connected to the CPLD chip.

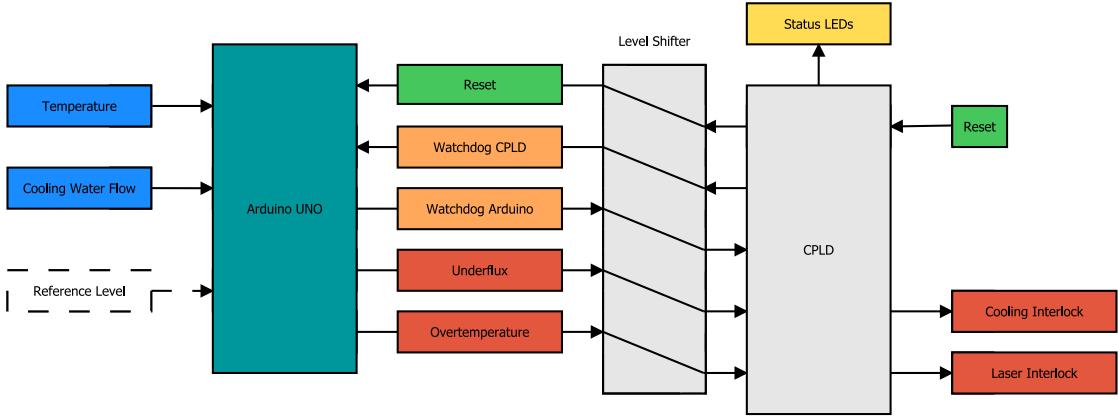


Figure A.1: Schematics of the interlock circuit. The level shifter has to be used to shift between the different logic levels (5 V for the Arduino, 3.3 V for the CPLD). It is also possible to set the reference level for the interlock by using a potentiometer (currently not used).

¹¹<http://www.arduino.cc/en/Main/ArduinoBoardUno>